Computers and Fluids 238 (2022) 105376

Contents lists available at ScienceDirect

Computers and Fluids

journal homepage: www.elsevier.com/locate/compfluid

Enhanced wickability of single-columnar, non-uniform pore-size wick using Lattice Boltzmann Method

Mohammad Borumand [a], Taehun Lee [b], Gisuk Hwang [a,*]

[a] Department of Mechanical Engineering, Wichita State University, Wichita, KS 67260, United States
[b] Department of Mechanical Engineering, The City College of New York, New York, NY 10031, United States

ARTICLE INFO

Keywords:
Rate-of-rise
Permeability
Capillary flow
Effective capillary meniscus radius
Graded porous media
Two-phase flow

ABSTRACT

Optimal wick designs are essential to develop high heat flux two-phase thermal management systems in various applications including miniaturized power electronics, energy, high power battery, and spacecraft systems, as they require both large permeability and improved capillary pressure, i.e., enhanced wickability. The enhanced wickability is examined using non-uniform pore size wicks, while the larger pores increase the permeability and the smaller pores improve the capillary pressure. A two-phase single component free-energy-based Lattice Boltzmann Method (LBM) is employed to study the enhanced wickability, i.e., pore-scale rate-of-rise through wicks. The rate-of-rise is predicted for uniform and non-uniform pore size wicks having a single-column-particle between the two parallel plates for given porosities ($\varepsilon = 0.67$ and 0.8) and pore size ratios ($l_r = 1.3$ and 2.6). The study shows that the non-uniform pore size wicks enhance the rate-of-rise and capillary pressure up to 298 and 157%, respectively, compared to those of the uniform pore size wicks, by improving the permeability through larger pores and increased capillary pumping capability through smaller pores. Also, the wickability enhances as the pore size ratios increase at given porosity or the porosity decreases at given pore size ratio. The cumulative enhancements of the maximum/minimum dimensionless liquid heights and the liquid saturation of non-uniform pore size wick are found to be up to 90, 114, and 112%, respectively, at $\varepsilon = 0.67$ and $l_r = 2.6$. The capillary pressure enhancement of non-uniform particle size wicks results from the presence of the small pores. Also, the vertically graded wicks increase the capillary pressure due to the smaller pores at the top of the wicks, while they marginally decrease the rate-of-rise compared to the non-uniform pore size wicks at given porosity and pore size ratio. The simulation results provide insights into the optimal thin wick structures for high heat flux two-phase thermal management system by enhancing the wickability through the non-uniform pore sizes.

1. Introduction

As the high power electronic and energy conversion systems miniaturize, the need for efficient, compact high heat flux thermal management systems become increasingly important for desired operation conditions [1,2]. Two-phase cooling systems such as heat pipes and vapor chambers offer high heat flux thermal management by using a latent heat compared to conventional single-phase cooling systems. A key design element is a wick structure which supplies a coolant to the heated surface via a capillary flow. However, the maximum cooling power, i.e., heat flux, is limited by the coolant chocking via a viscous-capillary limit where the viscous pressure drop reaches the capillary pumping capability [3].

The viscous-capillary limit is related to the absolute permeability and effective pore size of the wick structure, which are a function of the porosity, tortuosity, and pore size. In uniform pore size wick, such coupled relations have been extensively studied in meshes [4–6], sintered particles [7–10], and grooves [11,12]. To improve the viscous-capillary limit, i.e., the maximum heat flux, various non-uniform wicks have been examined. Semantic and Catton [13] have studied the enhanced pool boiling performance of bi-porous wicks and reported 73% Critical Heat Flux (CHF) enhancement for the thin wicks compared to mono-porous wicks. The CHF enhancement is related to the combined effects of the continued liquid supply and increased active evaporating capillary menisci of the bi-porous wick. Byon and Kim [14] have developed a semi-analytic model to predict and optimize the enhanced wickability (K/r_{eff}) of bi-porous wicks and reported up to 11 times wickability enhancement compared to the mono-porous wicks. Albu et al [15]. have experimentally characterized the rate-of-rise of the

* Corresponding author.
E-mail address: Gisuk.Hwang@wichita.edu (G. Hwang).

https://doi.org/10.1016/j.compfluid.2022.105376
Received 11 August 2021; Received in revised form 23 January 2022; Accepted 25 February 2022
Available online 2 March 2022

Nomenclature

Bo	Bond number
c_s	speed of sound
D	liquid-vapor interface thickness
d_p	average particle size
E_0	bulk free energy
e	microscopic particle velocity vector
F	intermolecular interaction force
f_α	distribution function
f_α^{eq}	equilibrium distribution function
g	gravitational acceleration
h	liquid height
h_0	liquid submerged depth
h_1	liquid depth
h^*	dimensionless liquid height
K	permeability
L_c	capillary length
l_p	characteristic pore size
l_r	pore size ratio
LP	large pore
Oh	Ohnesorge number
w	parameter for contact angle calculation
r_c	capillary meniscus radius
r_p	particle radius
s	liquid saturation
SP	small pore
p	pressure
t	time
t^*	dimensionless time
u, U	macroscopic velocity
UP	uniform pore
W	plate spacing
w_1	liquid reservoir width

Greek symbols

ρ	density
σ	surface tension
δ	parameter for contact angle calculation
δ_x	x-direction lattice spacing
δ_y	y-direction lattice spacing
δ_t	time spacing
λ	relaxation time
τ	dimensionless relaxation time
μ	dynamic viscosity
η	chemical potential
κ	gradient parameter
β	constant
θ	contact angle
ε	porosity
Ω	dimensionless wetting potential
α	angle related to equilibrium contact angle
ϕ	constant related to density on solid surface
ψ	mixing energy density
ξ	maximum instantaneous enhancement of non-uniform wick
ω	cumulative enhancement of non-uniform wick
γ	capillary pressure enhancement of non-uniform wick

subscripts

c	capillary, contact angle
d	dynamic
eq	equilibrium
ext	outer surface of the parallel plates
l	liquid
nu	non-uniform
p	particle or pore
s	surface
sat	saturation
u	uniform
v	vapor

bi-particle size thin sintered wicks and achieved wickability enhancement. Egbo et al [16]. have measured the phase-change heat transfer of the non-uniform wicks, enhancing CHF up to 1.48 times compared to the uniform wick depending on the wick thickness, particle size, and wick superheat. They concluded that the enhanced wickability of the non-uniform wick results from the simultaneous increase in the permeability and capillary pressure from the large and small pores, respectively. Zhou et al [17]. have measured the enhanced capillary and thermal performance of a novel bi-porous spiral woven mesh wick by using the advantage of large permeability, capillary force, and low cost of bi-porous wicks. Wang et al [18]. studied the effects of gradient porous media on fluid flow and heat transfer in microchannels to improve the heat transfer efficiency by adjusting the gradients of pore size or porosity of porous architecture. Dai et al [19]. studied the effects of porosity and pore size arrangement on themohydraulic performance of graded microchannel with microencapsulated phase change material, i.e., linear and stepwise increasing and decreasing porosity, however, their study mainly focused on a thermal resistance analysis without analyzing wickability enhancement. Although the previous studies have shown the enhanced wickability of the non-uniform pore size wicks, the pore-scale wickability enhancement mechanisms have still been poorly understood.

The Lattice Boltzmann Method (LBM) is an ideal simulation tool for pore-scale, two-phase flow in complex geometries such as the wick structures [20,21], due to the convenient boundary condition implementations of complicated porous media and low computational costs compared to the Level Set Method (LSM) [22] and the Volume of Fluid (VOF) [23] methods. However, the previous LBM studies have focused on single-phase flow [24,25], or considered the capillary flow only in fibrous pore networks [26]. Hoef et al [24]. have examined the permeability and drag force of low Reynolds-number gas flow over mono- and bi-disperse arrays of spheres using single-phase LBM. Pan et al [27]. have examined single-phase flow through two 3D porous media-a body-centered cubic array of spheres and a random-sized sphere-pack-and studied the effects of the LBM simulation parameters such as the lattice size, relaxation time, and fluid-solid boundary condition schemes on the accuracy of the flow simulation including viscosity-dependent permeability. Dorai et al [25]. have studied the single-phase flow through a packed bed of cylindrical particles including the effects of particle shape and polydispersity on pressure drop. Nabovati et al [26]. have developed a 3D single-phase LBM to study fluid flow in random fibrous porous media over a wide range of void fractions and permeability using the Darcy law. Khabbazi and Bazylak [28] have employed a single-phase LBM to calculate the absolute permeability of two simulated porous structures: periodic arrays of (a) staggered parallel infinite cylinders and (b) spheres and predicted the Kozeny–Carman porosity-permeability relationship for the geometries examined. Gharibi et al [29]. have combined LBM and Smoothed Profile Method (SPM) to simulate the single-phase flow in granular porous media and investigated the effects of porosity, particle size and shape, and the structure of porous media on the permeability and drag coefficient. Luo et al [30]. developed a single-phase LBM to study a novel Leaf-vein-inspired

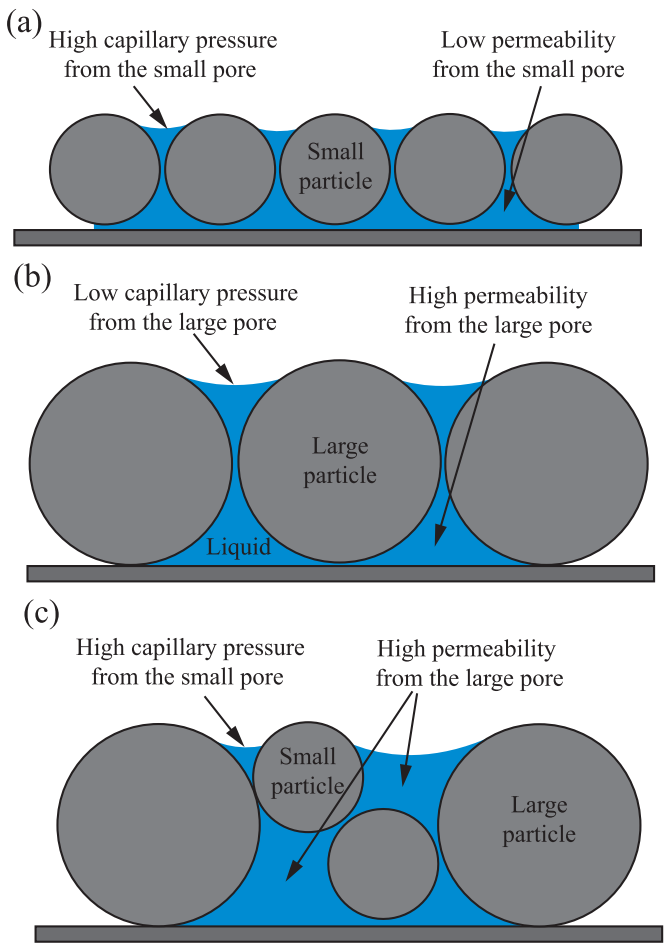

Fig. 1. Schematic of the liquid-filled sintered particle wick with (a) uniform small particle (or pore), (b) uniform large particle (or pore), and (c) non-uniform particle (or pore). Uniform and non-uniform capillary meniscus radii are also shown.

Table 1
LBM simulation parameters.

LBM Parameter	Magnitude in Lattice Unit
δ_x	1
δ_x	1
δ_t	1
ρ_l^{sat}	1
ρ_v^{sat}	0.2
θ_{eq}	30°
c_s	$1/\sqrt{3}$
λ	0.5
σ	1.365×10^{-3}
β	0.01
κ	0.0128
D	4
h_0	75
h_1	200
w_1	400
W	100

Gradient Porous (LGP) wick structure by comparing the contours of velocity magnitude and temperature between LBM and Finite Volume Method (FVM) simulations and illustrated the superior flow and heat transfer performance of the LGP wick.

Huang et al [31]. have extended the LBM boundary condition for single phase flow to simulate immiscible two-phase displacement in complex heterogeneous porous media with significantly reduced

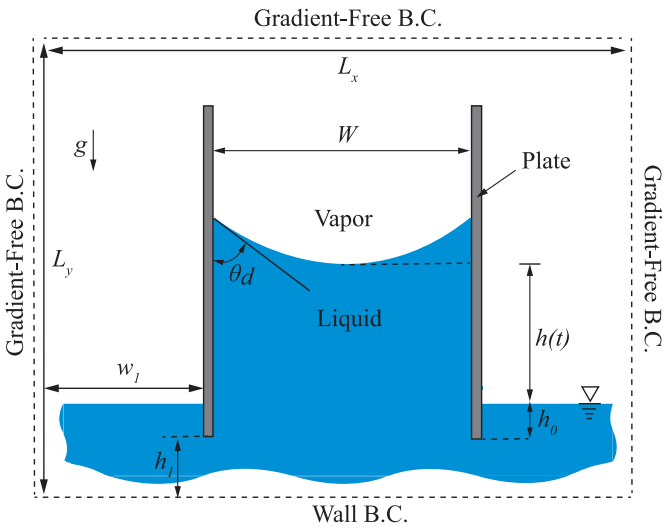

Fig. 2. Rate-of-rise between two parallel plates in contact with a liquid reservoir (Case 0). Liquid, vapor, plates, space between the plates, W, liquid height, h, liquid-submerged depth, h_0, liquid depth, h_1, liquid reservoir width, w_1, dynamic contact angle θ_d, gravitational acceleration, g, and domain size, L_x and L_y are also shown.

Table 2
Summary of the LBM simulation parameters for two parallel plates (Case 0).

Simulation parameter	Magnitude, Lattice Unit (Case 0)
W	100
$g\times10^7$	4.55
L_x	910
L_y	600

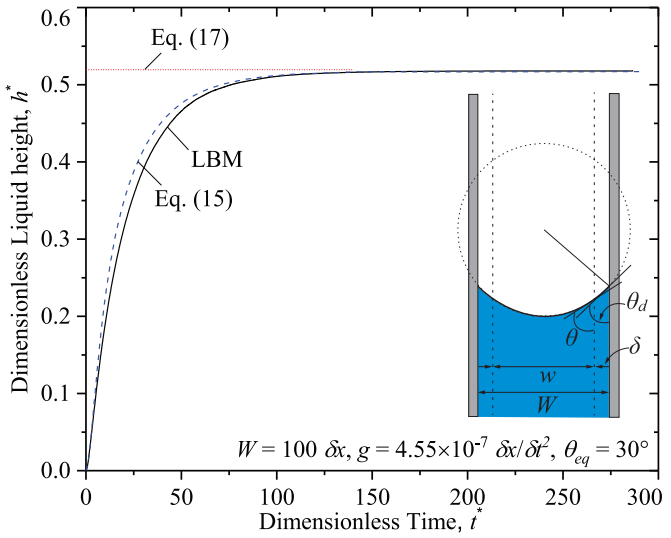

Fig. 3. Predicted LBM results for the rate-of-rise between parallel plates (Case 0) with $W = 100\ \delta x$, $\theta_{eq} = 30°$, and $g = 4.55\times10^{-7}\ \delta x/\delta t^2$, compared with closed-form solution, i.e., the Bosanquet equation, Eq. (15). The predicted liquid height at equilibrium, h_{eq} using Eq. (17) is also shown. The dynamic contact angle, θ_d, for Eq. (16) is also shown.

spurious currents and better numerical stability and obtained the three typical flow patterns, namely stable displacement, viscous fingering, and capillary fingering, over a wide range of capillary numbers and viscosity ratios. Liu et al. [32,33] simulated immiscible two-phase flow in homogeneous and heterogeneous pore networks using LBM and studied

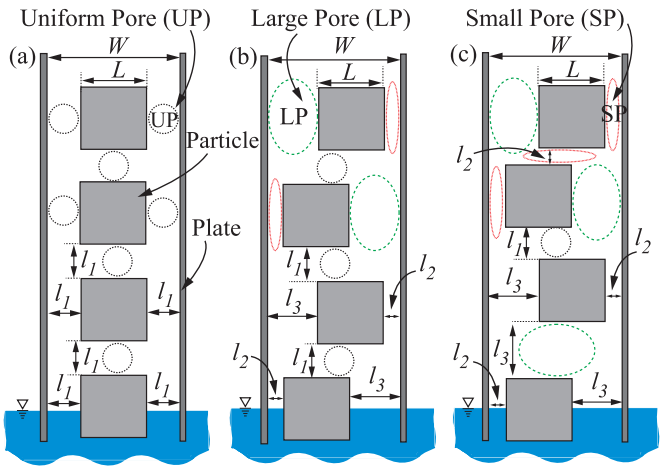

Fig. 4. Single-column, particle wicks between two parallel plates with the spacing of W for (a) Uniform Pores (UPs) (Cases A1 and B1), (b) non-uniform pores (horizontal rearrangement only, Cases A2, A3, B2, and B3), (c) non-uniform pores (horizontal/vertical rearrangements, Cases A4 and B4). The plate spacing, W, square particles sizes, L, and pore sizes (l_1 to l_3) including the Uniform Pores (UP), Small Pores (SP), and Large Pores (LP) are also shown. The contact angle θ_c, domain sizes (W, h_1, h_0, w_1, L_x and L_y), and the bounadry conditions are the same as those of Fig. 2.

Table 3
Summary of the LBM simulation parameters for uniform and non-uniform single-column particle wick shown in Fig. 4(a)-(d) with two different porosities, $\varepsilon = 0.67$, and 0.8. The parallel plate spacing and gravitational acceleration are $W = 100\ \delta x$ and $g = 1.4 \times 10^{-7}\ \delta x/\delta t^2$, respectively. The domain sizes h_1, h_0, w_1, L_x, and L_y are same as those of Table 2.

	Magnitude, Lattice Unit					
Simulation parameters	Case A1	Case A2	Cases A3, A4	Case B1	Case B2	Cases B3, B4
ε	0.67	0.67	0.67	0.8	0.8	0.8
L	50	50	50	36	36	36
l_1 (UP)	25	25	25	32	32	32
l_2 (SP)	–	22	14	–	28	18
l_3 (LP)	–	28	36	–	36	46
$l_r = l_3 / l_2$ or l_1/l_1	1	1.3	2.6	1	1.3	2.6

the effects of flow properties such as the capillary number, viscosity ratio, surface wettability, and porous media heterogeneity on the patterns of the three typical wetting fluid displacement. Huang et al [34]. have also studied two-phase immiscible displacements in randomly-packed spheres and characterized the effects of capillary number, viscosity ratio, and wettability on the dynamics of displacement and the relative permeability. Falcucci et al [35]. have employed the LBM to study the pulsed reactive flows in transitional Knudsen number regimes. They have characterized the conversion efficiency of catalytic particles for different geometries and configurations, including single catalytic particle and nanoporous gold spheres, within pulsed-flow reactors. Montemore et al [36]. have utilized a multi-component LBM to explore the possibility of oxidation reactions on nanoporous gold, an AgAu bimetallic catalyst using microscopy and image reconstruction to obtain the morphology of a two-dimensional slice of a nanoporous gold sample. Li et al [37]. have used a 2D pore-scale, two-phase LBM to study the dynamics of simultaneous flow of immiscible two-phase fluids at the steady state in the capillary force-dominated regime by calculating the capillary pressure and relative permeability as a function of fluid saturation. Wang et al. [38] have investigated the immiscible displacement in porous media with the displaced fluid being shear-thinning using a two-phase LBM and explored the influence of the heterogeneous viscosity field on viscous fingering. Gu et al [39]. have studied the pore-scale, spontaneous liquid imbibition through an oil-saturated artificial 2D porous matrix for oil recovery applications by employing color-gradient, two-phase (water--oil) LBM. Falcucci et al [40]. have used the LBM-based extreme flow simulations to study flow in deep-sea glass sponges with highly complex porous geometry. Li et al. [41] have examined the capillary pumping processes of the reconstructed random porous wicks at pore scale by using a 3D two-phase LBM. They have also investigated the evolutions of two-phase interface and the variations of the transient imbibed liquid volume fraction for the different porosity, pore structure, and surface wettability to compare with the macroscopic scale homogenous model. However, the pore-scale capillary flow in the non-uniform thin wick have been still poorly understood, mainly due to the expensive computational cost. Recently, Borumand et al. [42] have studied the enhanced wickability of non-uniform wicks using LBM, and they primarily focused on pore-scale enhanced capillary flows through the non-uniform pore-size distributions.

In this study, the tailored capillary flow in non-uniform thin wick is examined using two-phase free-energy-based LBM, aiming at understanding the enhanced wickability including porosity, pore size distribution, and pore size ratio effects Section 2. discusses the working principles of enhanced wickability in non-uniform wick, and Section 3 describes the LBM and simulation details Section 4. includes the LBM validation and predicted rate-of-rise in uniform and non-uniform thin wicks, followed by the conclusion in Section 5.

2. Working principles

The optimal wick structure requires both the large permeability and capillary pressure for the development of the high heat flux two-phase cooling system. However, the wick permeability, K is proportional to the particle size squared, as given as [2]

$$K = a\frac{\varepsilon^3 {r_p}^2}{(1-\varepsilon)^2} \tag{1}$$

where ε is the porosity, a is the constant, and r_p is the particle radius, while the capillary pressure, p_c is inversely proportional to the capillary meniscus radius (or particle size) as given as [2]

$$p_c = \frac{2\sigma\cos(\theta)}{r_c} \tag{2}$$

where σ is the surface tension, θ is the contact angle, and r_c is the capillary meniscus radius. In other words, it is challenging to simultaneously increase the permeability and capillary pressure using the uniform particle size (or characteristic pore size). To overcome this challenge, the non-uniform particle size wick is employed to achieve the increased capillary pressure from the small particle size and the large permeability from the large particle [43,44] as shown in Fig. 1.

Fig. 1(a) shows that the small uniform pore size wick suffers from the low permeability, while Fig. 1(b) illustrates the poor capillary pressure in the large uniform pore size wick. However, the combination of the small and large pores, i.e., the non-uniform pore size wick shown in Fig. 1(c), can lead to the simultaneous enhancement of permeability and capillary pressure. Note that Fig. 1 schematically shows the working principle based on sintered-particle wick, however, we employ a simple 2D non-uniform pore size wick with non-uniform rectangular pore size between the two parallel plates to fundamentally understand the enhanced wickability without losing a generality. The details of various non-uniform pore arrangements are found in Section 3.3.

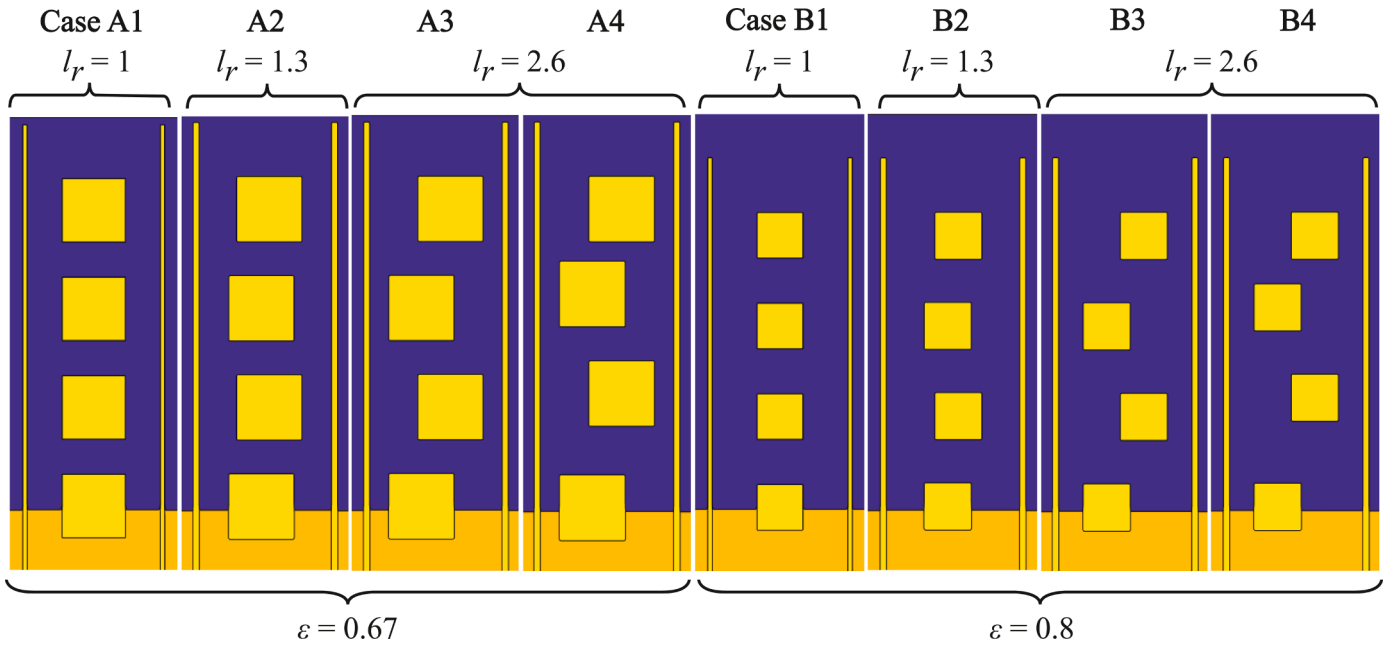

Fig. 5. Snapshots of all single-column particle wicks at $t^* = 0$. The uniform pore wicks, i.e., Cases A1 and B1 [see Fig. 4(a)], non-uniform pore wicks with horizontal rearrangement, i.e., Cases A2-A3 and Cases B2-B3 [see Fig. 4(b)], and non-uniform pore wicks with horizontal and vertical rearrangements, i.e., Cases A4 and B4 [see Fig. 4(c)] are shown. The porosity and pore size ratio, i.e., ε and l_r, are also shown.

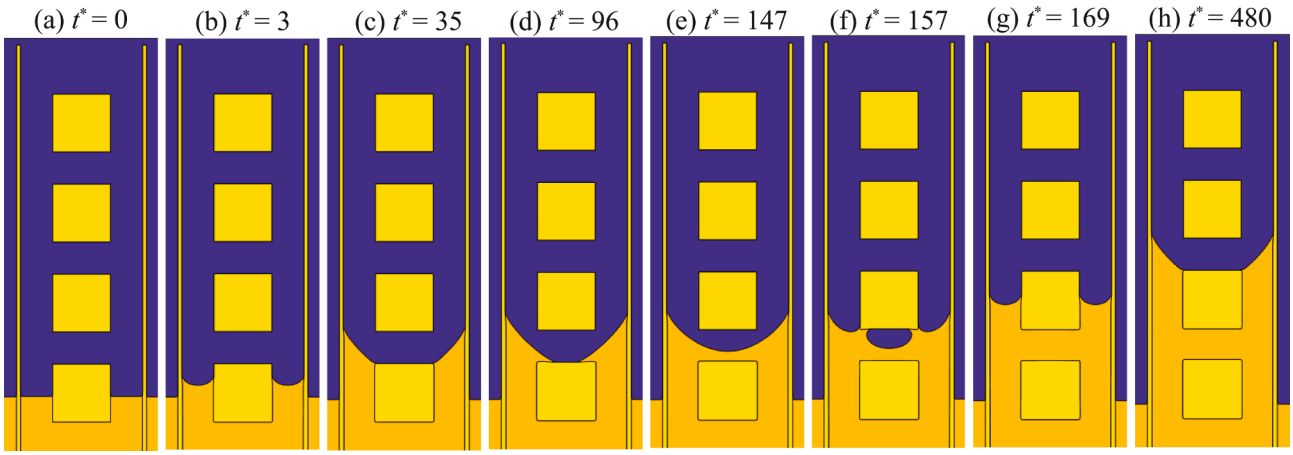

Fig. 6. Snapshots of rate-of-rise in single-column-particle uniform pore size wick with $\varepsilon = 0.67$ (Case A1) from (a) the initial time, $t^* = 0$, to (h) the equilibrium condition $t^* = 480$. Given dimensionless time, t^*, for each snapshot is also shown.

3. LBM simulation

3.1. Lattice Boltzmann Method (LBM)

To simulate the pore-scale capillary flow in the single column particle wicks, a two-phase single component free-energy-based LBM is used. In this paper, only the key governing equations and approaches are given, and the details are found in the previous works [45–47]. The discrete Boltzmann equation (DBE) for the van der Waals fluid using Bhatnagar–Gross–Krook (BGK) collision operator can be written as [48]

$$\frac{\partial f_\alpha}{\partial t} + \mathbf{e}_\alpha \cdot \nabla f_\alpha = -\frac{f_\alpha - f_\alpha^{eq}}{\lambda} + \frac{(\mathbf{e}_\alpha - \mathbf{u})\cdot\mathbf{F}}{\rho c_s^2} f_\alpha^{eq} \tag{3}$$

where f_α is the single-particle distribution function, $\mathbf{e}_\alpha$ is the microscopic velocity f^{eq} is the equilibrium distribution function, λ is the relaxation time due to collision, $\mathbf{u}$ is the macroscopic velocity, ρ is the density, c_s is the speed of sound, and $\mathbf{F}$ is the averaged external force experienced by each particle, i.e., intermolecular interaction force. Note that $c_s = c/\sqrt{3}$, where $c = \delta_x/\delta_t$ is the lattice speed, and δ_x, δ_y, and δ_t are unity, respectively. The D2Q9 scheme is chosen for this study. To minimize the parasitic currents, which are small-amplitude velocity fields at the phase interface arising from imbalance between thermodynamic pressure-gradient term and the interfacial stress term as a result of truncation error [45,49], so called potential forcing scheme, is used to eliminate the parasitic currents to round-off, which is given as

$$\mathbf{F} = \nabla\left(\rho c_s^2\right) - \rho\nabla\left(\mu_0 - \kappa\nabla^2\rho\right) \tag{4}$$

The chemical potential, μ_0, and the gradient parameter, κ, can be found using Eqs. (5) and (6), respectively

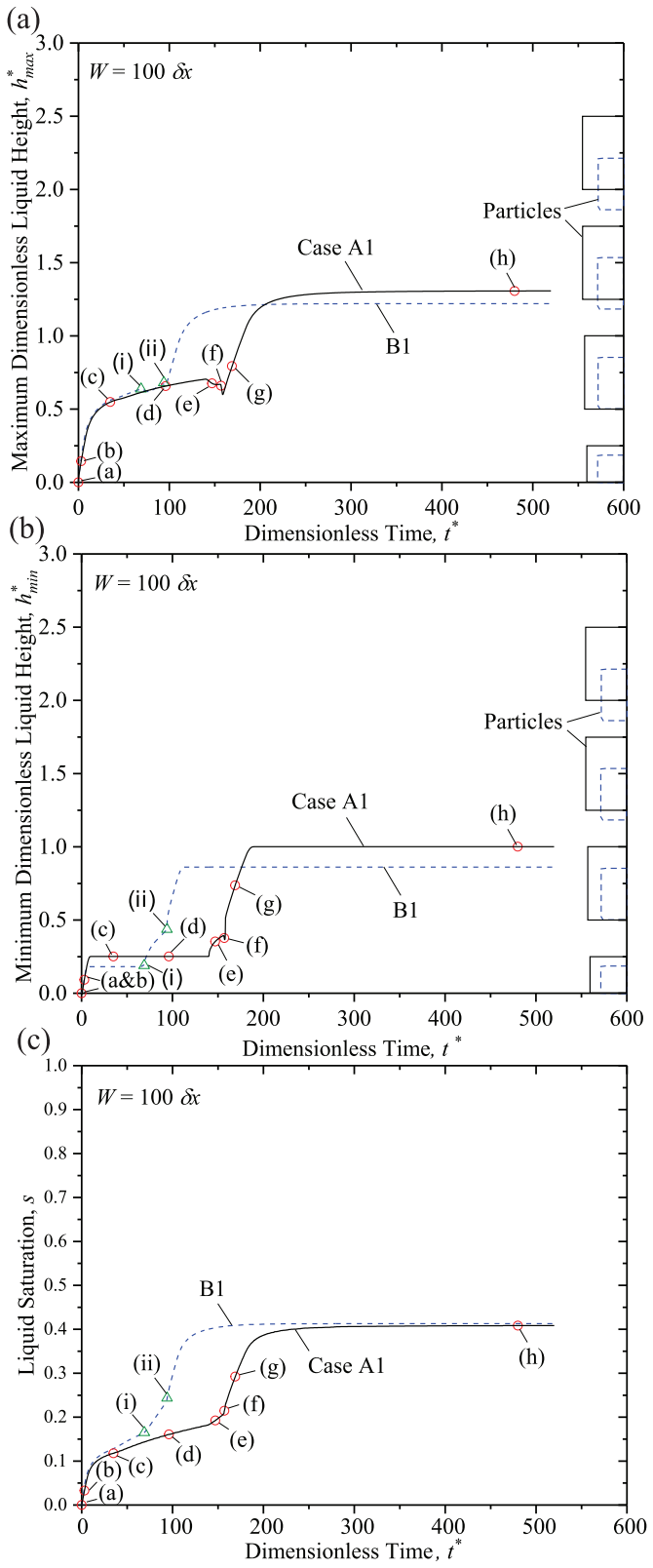

Fig. 7. (a) Maximum dimensionless liquid height, h_{max}*, (b) minimum dimensionless liquid height, h_{min}*, and (c) liquid saturation, s, as a function of dimensionless time, t*, for uniform wick with $\varepsilon = 0.67$ (Case A1) and $\varepsilon = 0.8$ (Case B1). The time-label for the rate-of-rise snapshots shown in Fig. 6(a)–(h), the location of the 4 particles for Cases A1 and B1, and the plate spacing, W, are also shown.

$$\mu_0 = \frac{\partial E_0}{\partial \rho} \tag{5}$$

$$\kappa = \frac{\beta D^2 \left(\rho_l^{sat} - \rho_v^{sat}\right)^2}{8} \tag{6}$$

where E_0 is the bulk free energy, ρ_l^{sat} and ρ_v^{sat} are the liquid and vapor densities at saturation, respectively, β is a constant related to the compressibility of the bulk phase, and D is the interface thickness which should be greater than 3 lattices to avoid numerical instability. Here, $D = 4$ and $\beta = 0.01$ are used. Given κ and β, surface tension can be computed as

$$\sigma = \frac{\left(\rho_l^{sat} - \rho_v^{sat}\right)^3}{6}\sqrt{2\kappa\beta} \tag{7}$$

An approximation for the bulk free energy E_0 can be expressed in the vicinity of the critical point by simplifying the equation of state, resulting in

$$E_0(\rho) = \beta\left(\rho - \rho_v^{sat}\right)^2\left(\rho - \rho_l^{sat}\right)^2 \tag{8}$$

To find the total free energy of an isothermal thermodynamic system that contains wall boundaries, Eq. (9) is used

$$\Psi_b + \Psi_s = \int_\Omega \left(E_0(\rho) + \frac{\kappa}{2}|\nabla\rho|^2\right)d\Omega - \int_\Gamma \varphi_1 \rho_s d\Gamma \tag{9}$$

where ψ_b is the mixing energy density, ρ_s is the density at the solid surface, and ψ_b is the wall energy density that contains only the linear term [46]. The relation between φ_1 in Eq. (9), the dimensionless wetting potential Ω, and the equilibrium contact angle θ_{eq} can be expressed by

$$\Omega = \frac{4\varphi_1}{\left(\rho_l^{sat} - \rho_v^{sat}\right)^2}\sqrt{2\kappa\beta} \tag{10}$$

$$\Omega = 2\mathrm{sgn}\left(\frac{\pi}{2} - \theta_{eq}\right)\left(\cos\left(\frac{\alpha}{3}\right)\left[1 - \cos\left(\frac{\alpha}{3}\right)\right]\right)^{\frac{1}{2}} \tag{11}$$

where

$$\alpha = cos^{-1}\left(\sin\theta_{eq}\right)^2 \tag{12}$$

The boundary condition at the wall for $\nabla^2\rho$ in Eq. (4) takes the form of

$$\kappa \mathbf{n}\cdot\rho_s = -\phi_1 \tag{13}$$

where $\mathbf{n}$ is the unit vector normal to the wall. Therefore, $\mu = \mu_0 - \kappa\nabla^2\rho$ in Eq. (4) can be treated as a scalar, discretized in like manner, and this results in the elimination of the parasitic currents at the phase interface.

Table 1 summarizes the values of the LBM parameters used in the present study.

To find the unknown particle distribution at the wall, equilibrium boundary condition is implemented in which ρ_s is calculated based on the bounce back rule after streaming step followed by immediate relaxation toward the equilibrium state [46,50]. Therefore, the density ρ and chemical potential μ at the wall boundary should be calculated using

$$\begin{aligned}\phi(\mathbf{x}_s + \mathbf{e}_\alpha\delta t) &= \phi(\mathbf{x}_s - \mathbf{e}_\alpha\delta t)\\ \phi(\mathbf{x}_s + 2\mathbf{e}_\alpha\delta t) &= \phi(\mathbf{x}_s - 2\mathbf{e}_\alpha\delta t)\end{aligned} \tag{14}$$

where ϕ stands for ρ or μ, $\mathbf{x}_s$ represents the wall node, and δ_t is the time step. However, the special wall boundary treatment is needed at the sharp corners of solid particles and surfaces due to the unavailability of the explicit normal vector. In this study, the isotropic method is used [47].

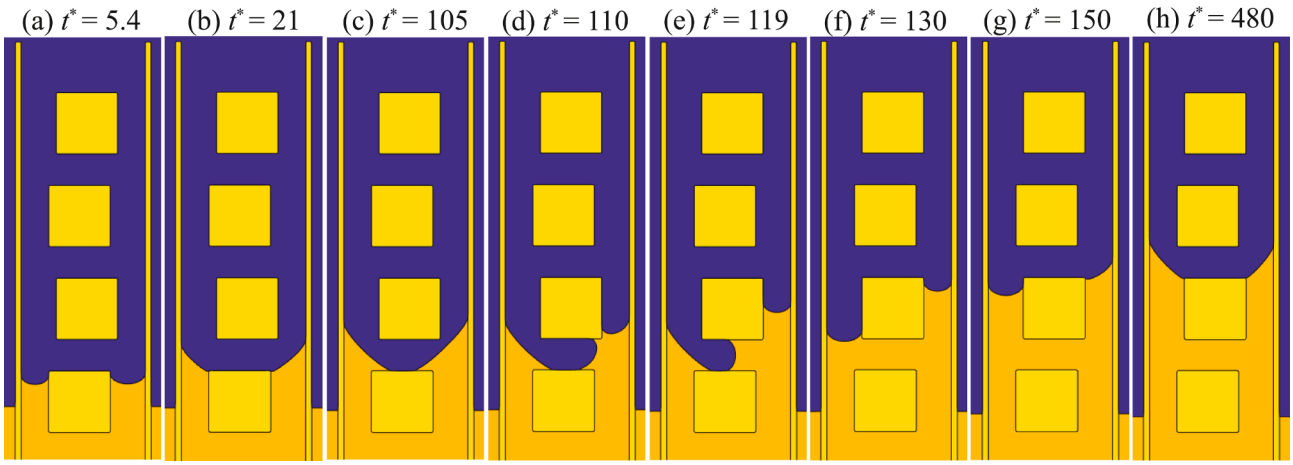

Fig. 8. Snapshots of rate-of-rise in single-column non-uniform pore size wick with $\varepsilon = 0.67$ and $l_r = 1.3$ (Case A2) from (a) $t^* = 5.4$ to (h) the equilibrium state $t^* = 480$. The dimensionless time, t^*, corresponding to each of the snapshots are also shown.

3.2. Rate-of-rise in two parallel plates

To validate the LBM, the rate-of-rise between the two parallel plates using the LBM are compared with the closed-form solution, so called Bosanquet equation [51], given as

$$\left(h^* + h_0^*\right)\frac{d^2h^*}{dt^{*2}} + \left(\frac{dh^*}{dt^*}\right)^2 + \left(h^* + h_0^*\right)\frac{dh^*}{dt^*} = a\cos\theta_d - bh^* \tag{15}$$

where $h^*=h(t)/W$ and $h_0^*=h_0/W$ are dimensionless liquid height above the liquid-vapor surface and dimensionless liquid-submerged length, respectively, as shown in Fig. 2. The W, g, and σ are the parallel plate spacing, gravitational acceleration, and surface tension, respectively, $\theta_d = \theta_d(t)$ is the dynamic contact angle, $t^* = t/t_0$ is the dimensionless time, and $t_0 = \rho_l (W^2)/12\mu_l$, $a = 2\rho_l (W)\sigma/(12\mu_l)^2$ and $b = \rho_l^2 (W)^3 g/(12\mu_l)^2$. Note that the dimensionless liquid height, h^* in the LBM predicts the maximum (capillary meniscus liquid front near the plate) and the minimum heights (central part of the capillary meniscus recess), and only minimum height is shown in Fig. 2. The dynamic contact angle is calculated using

$$\theta_d = \frac{\pi}{2} - \sin^{-1}\left\{\frac{W}{w}\sin\left[\frac{\pi}{2} - \theta(\delta)\right]\right\} \tag{16}$$

where $\theta(\delta)$ is the contact angle calculated at the distance δ from the internal plate surface [52] Table 2. summarizes the LBM simulation parameters including the equilibrium contact angle, θ_{eq}, parallel plates spacing, W, gravitational acceleration, g, the reservoir liquid depth, h_1, the parallel plates submersion length, h_0, the domain size from the side boundaries to the external surface of the plates, w_1, and the overall domain sizes in both directions, L_x and L_y, as shown in Fig. 2. The Bosanquet equation was solved using 4th order Runge-Kutta method. The liquid height at equilibrium, h_{eq}, can be found given as

$$\rho_l g h_{eq} = \frac{2\sigma\cos(\theta)}{W} \tag{17}$$

3.3. Rate-of-rise in two parallel plates (Validation of LBM simulation)

The LBM simulation predicts the rate-of-rise between two parallel plates (see Fig. 2) and compares with the closed-form solution, i.e., the Bosanquet equation, Eq. (15) for validation as shown in Fig. 3, showing RMS error below **2%**. Note that the LBM simulation and Eq. (15) use $W = 100\ \delta x$, $\theta_{eq} = 30^\circ$, and $g = 7\times10^{-7}\ \delta x/\delta t^2$, and Fig. 3 shows the rate-of-rise only after the liquid-vapor meniscus is fully formed at $t^* = 0$. The LBM-predicted rate-of-rise sharply increases at $t^* < 100$, and it reaches plateau as it approaches the equilibrium height. The LBM-predicted equilibrium height agrees the closed form solution, Eq. (17).

3.4. Single-column, uniform and non-uniform pore size wicks

To investigate the effects of non-uniform pore size distribution on the enhanced wickability, the rate-of-rise in the single-column particle wicks with uniform and non-uniform pore size distributions are simulated using LBM, as shown in Fig. 4(a)–(c) Fig. 4.(a) illustrates the parallel plates with the spacing of W and the single-column square particles, where the pore sizes are uniform near the particles, i.e., Uniform Pore (UP) (Cases A1 and B1 at $\varepsilon = 0.67$ and 0.8, respectively).

For the non-uniform pore size wicks, three particle arrangement variations are examined Fig. 4.(b) shows the horizontal particle rearrangements only to create the smaller, $l_2 < l_1$, and the larger pore sizes $l_3 > l_1$ for given parallel plate spacing, $W = 100\ \delta x$, and porosity (Cases A2 and A3 with $l_r = 1.3$ and 2.6, respectively, at $\varepsilon = 0.67$, and Cases B2 and B3 with $l_r = 1.3$ and 2.6, respectively, at $\varepsilon = 0.80$). Note that the first two bottom particles are served as a building block, the total four particles are used to ensure the enhanced wickability between the two building blocks. Furthermore, two different wick porosities, $\varepsilon = 0.67$ and 0.80, and two different pore size ratios, $l_r = 2.6$ and 1.3, are simulated to study the effects on the wickability enhancement. To understand the effects of the horizontal and vertical non-uniform pore sizes, Fig. 4(c) shows the horizontal/vertical particle rearrangements, i.e., additional vertical particle rearrangement compared to that shown in Fig. 4(b). This represents the Cases A4 with $l_r = 2.6$, respectively, at $\varepsilon = 0.67$, and Case B4 with $l_r = 2.6$, respectively, at $\varepsilon = 0.8$. To ensure the lattice size independent LBM simulations, the minimum pore size of 14 δx is used for all the LBM simulations as the details are found in Appendix. Note that the contact angle of $\theta_{c,\ ext} = 90^\circ$ is used for the outer wall, to prevent the liquid from forming the capillary meniscus at the outer wall Table 3. summarizes the LBM simulation parameters including the porosity, ε, particle size, L, the uniform pore size, l_1, the small pore size, l_2, and the large pore size, l_3, for the uniform and non-uniform wicks shown in Fig. 4.

Fig. 5 shows the LBM snapshots of the single-column particle wicks at $t^* = 0$ which includes wicks with lower porosity ($\varepsilon = 0.67$), i.e., Cases A1-A4, and Cases B1-B4 which have higher porosity, i.e., $\varepsilon = 0.8$. Cases A1- and B1 are uniform pore size wicks which correspond to Fig. 4(a), Cases A2 and B2, and Cases A3 and B3 are non-uniform pore wicks with low and high pore size ratios, i.e., $l_r = 1.3$ and 2.6, respectively, while Cases A4 and B4 are non-uniform wicks with high pore size ratio ($l_r = 2.6$) that have additional non-uniform pore distribution, i.e., decreasing

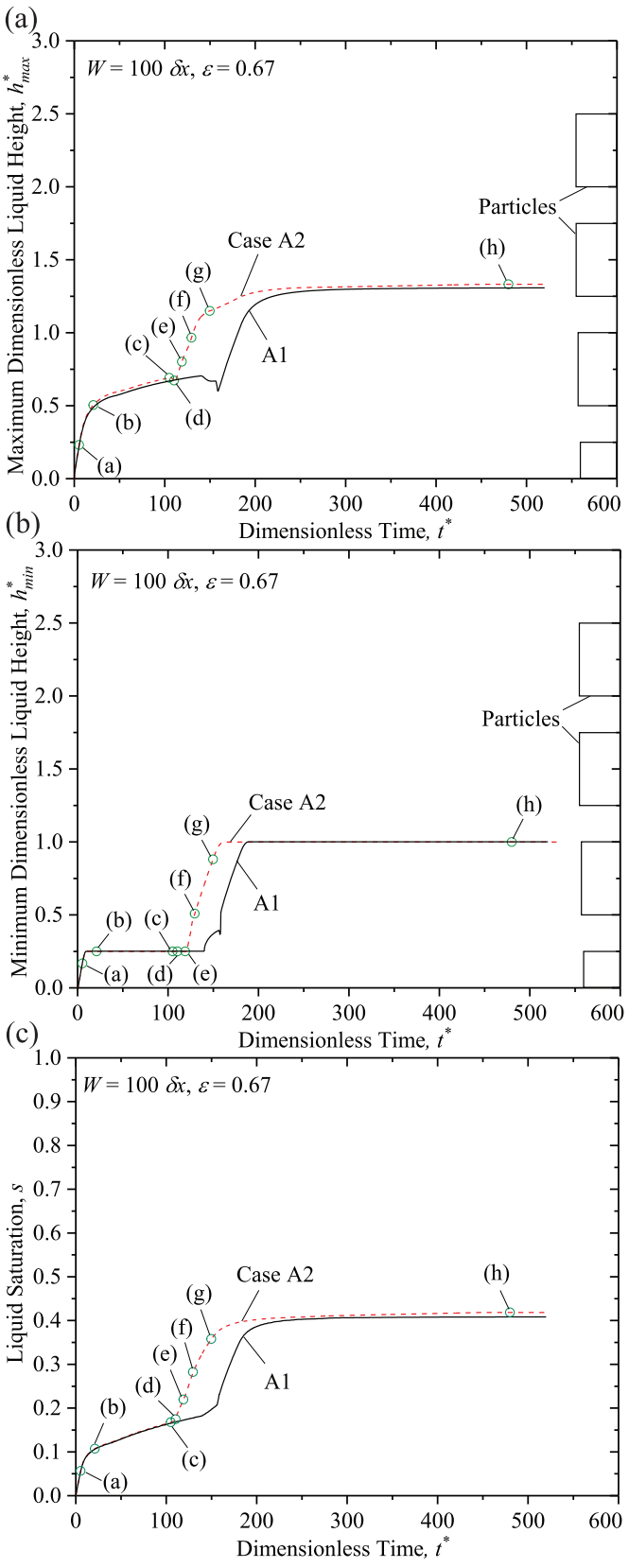

Fig. 9. (a) Maximum dimensionless liquid height, h_{max}*, (b) minimum dimensionless liquid height, h_{min}*, and (c) liquid saturation, s, as a function of dimensionless time, t*, for uniform (Case A1) and non-uniform wick (Case A2, l_r = 1.3) at given porosity (ε = 0.67) and parallel plate spacing (W = 100 δx).

pore size in the upward flow direction.

4. Results and discussion

The rate-of-rise through the single-column, uniform and non-uniform pore size wicks within the two parallel plates (see Fig. 4) are predicted using the LBM to understand the enhanced wickability of the non-uniform pore size wicks including the pore size distribution, pore size ratio, and porosity effects. The rate-of-rise is characterized by considering maximum dimensionless liquid height, h_{max}*, minimum dimensionless liquid height, h_{min}*, and liquid saturation, s. Note that all the LBM parameters are found in Tables 1 and 2, but a lower gravitational acceleration is used, i.e., $g = 1.4 \times 10^{-7}\ \delta x/\delta t^2$ to achieve the higher equilibrium height, i.e., the top layer of the wick. Note that the presence of the wicks particles between the two parallel plates reduces the effective pore size, which in turn results in the higher equilibrium height than that of the parallel plates only. However, the "true" equilibrium height cannot be predicted using analytical expression, i.e., Young-Laplace equation due to the unknown pinning effects at the sharp corner of the square particles. Thus, we adjust the gravity using a trial-and-error approach to maintain the equilibrium within the simulation domain. Two different porosities and pore size ratios are considered to study their effects on enhanced wickability, and three different non-uniform pore size distributions are studied as shown in Fig. 4(b)–(d).

4.1. Uniform pore size wick: porosity effect

Fig. 6 shows the LBM simulation snapshots of the rate-of-rise from the initial time to equilibrium state for the single-column-particle uniform pore size wick with ε = 0.67, i.e., Case A1 (see Fig. 5) Fig. 6.(a) shows the initial liquid height within the two plates, which stays in the same level as the liquid pool at t^* = 0 Fig. 6.(b) illustrates the formation of the first capillary meniscus between the particle and plates at t^* = 3 by equally filling the pore space between the particle and plates, which in turn results in the sharp rate-of-rise. At t^* = 35, Fig. 6(c) shows that the minimum liquid height sticks to the sharp upper corner of the first particle, while the maximum liquid height continues to rise along the inner plate surface, i.e., pining [53], and it delays the rate-of-rise. Note that the capillary meniscus radius gradually increases between t^* = 3 and 35, i.e., the capillary pressure decreases during the pinning process due to the increasing capillary meniscus radius. At t^* = 96, Fig. 6(d) shows that as the maximum liquid height increases above the threshold height, the minimum liquid height detaches from the upper particle-corner, i.e., depinning. Then, it begins to laterally spread over the top surface of the particle, i.e., stick-slip flow, without changing the minimum liquid height. At t^* = 147, Fig. 6(e) shows that the meniscus radius remains large during the stick-slip flow until the triple-phase fronts finally bridge to form the capillary meniscus across the two plates. At t^* = 157, Fig. 6(f) illustrates that the liquid begins to interact with the bottom side of the second particle to form the small capillary menisci, followed by the second sharp rate-of-rise between the particle and the plate at t^* = 169 [Fig. 6(g)]. The liquid continues to rise until it reaches the top surface of the second particle, and then it does not significantly change the height due to the meniscus pinning. At t^* = 480, Fig. 6(h) shows that the decreased capillary pressure due to the pinning is lower than the hydrostatic pressure, i.e., the liquid front has reached equilibrium state.

Fig. 7(a) and (b) shows the LBM predicted maximum and minimum dimensionless liquid heights, h_{max}*, and h_{min}*, respectively, as a function of dimensionless time, t*, for the single-column-particle uniform pore size wicks with two porosities, ε = 0.67 (Case A1) and 0.8 (Case B1), at given parallel plate spacing, W = 100 δx. The time label for the rate-of-rise snapshots given in Fig. 6(a)–(h) and the location of the 4 particles for Cases A1 and B1 are also shown [see Fig. 4(a)]. They show the sharp rate-of-rise at t^* = 0 [Fig. 6(a) or point (a)] and t^* = 3 [point (b)] by quickly forming the capillary meniscus between the particle and

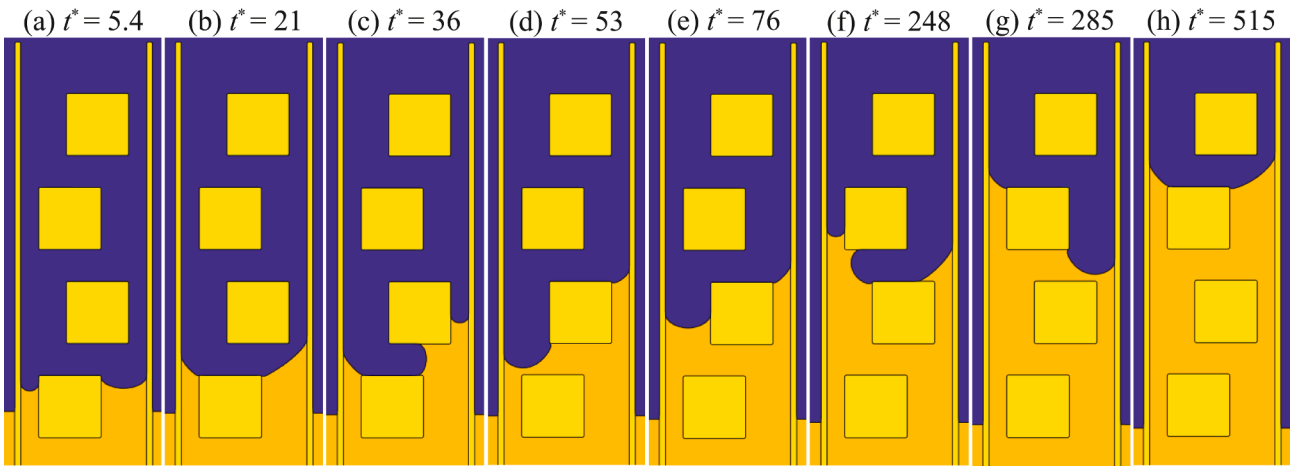

Fig. 10. Snapshots of rate-of-rise in single-column uniform pore size wick with $\varepsilon = 0.67$ and $l_r = 2.6$ (Case A3) from (a) $t^* = 5.4$ to (h) the equilibrium state at $t^* = 515$. The dimensionless time, t^*, corresponding to each of the snapshots are also shown.

plates, followed by a plateau due to the meniscus pinning at the upper particle-corner, i.e., point (c). During the pinning, the maximum height continues to rise along the inner plate surfaces, whereas the minimum heights do not change due to the pinning at the upper particle-corner. Once depinned from the particle corner, it initiates the stick-slip flow over the top surface of the first particle, i.e., point (d), until it bridges between two capillary menisci for another minimum liquid height step-wise rise, i.e., point (e). Note that the maximum liquid height decreases moderately and the minimum liquid height jumps due to the formation of the capillary meniscus across the two plates compared to the point (d). Then, the liquid front interacts with the two bottom corners of the second particle to form the three small capillary meniscus radii, i.e., point (f). At this point, due to the relocations of the capillary menisci, both the maximum and minimum liquid heights slightly decrease, followed by the second sharp rate-of-rise between the particle side walls and the plates inner surfaces, i.e., point (g). The liquid rises until it reaches the same level of the second particle top surface, where the maximum dimensionless liquid height gradually increases along the plate inner surface while the minimum dimensionless liquid height remains unchanged due to the pinning at the particle corner. At point (h), i.e., $t^* = 480$, the maximum dimensionless liquid height has reached the equilibrium state. For Case B1, a similar first step-wise, rate-of-rise is observed both for maximum and minimum liquid heights, but Case B1 shows the early second sharp rate-of-rise due to the larger pore size between the particle and inner plate surfaces, i.e., earlier formation of the capillary meniscus across the two plates after the stick-slip flow regime, and earlier liquid front interaction with the two bottom corners of the second particle, as indicated at (i) and (ii), respectively. Note that in terms of capillary meniscus front shape, (i) and (ii) are similar to points (e) and (f) in Fig. 6, respectively, i.e., meniscus formation between the parallel plates and meniscus interaction with the next particle, respectively.

Fig. 7(c) shows the liquid saturation, s, for Cases A1 and B1, to predict the rate-of-rise by characterizing the average liquid height. The larger porosity wick, i.e., Case B1, allows for the early step-wise liquid height increase compared to that of Case A1, indicating that the increased permeability by the larger pores outperforms the reduced capillary pressure by the smaller pores. Note that in Fig. 7(a) and (b), the maximum and minimum liquid equilibrium heights for Case A1 is slightly higher than that of Case B1 because the top surface of the second particle of Case A1 is placed higher than that of the Case B1, i.e., the larger particle size of Case A1. However, Fig. 7(c) shows that the liquid saturation at equilibrium is similar for both cases, indicating that the relative liquid filling is the same.

4.2. Non-uniform pore size wicks

The enhanced wickability of the non-uniform wick is investigated by comparing the rate-of-rise between the single-column-particle uniform (Case A1, $l_r = 1$) and non-uniform pore size (Case A2, $l_r = 1.3$) wicks at $\varepsilon = 0.67$ [see Fig. 5] Fig. 8.(a)–(h) shows the pore-scale capillary meniscus front movement of the non-uniform wick (Case A2). At t* = 5.4, Fig. 8(a) shows that the liquid level during the first sharp rate-of-rise is similar between the small and large pores, since the pore size ratio is relatively small, i.e., $l_r = 1.3$. During the meniscus pinning, subsequent depinning, and the following stick-slip flow as shown in Fig. 8(b) and (c), i.e., $t^* = 21$ and 105, the maximum liquid level is higher in the large pore due to the extended meniscus crescent in the larger pore. At $t^* = 110$, Fig. 8(d) shows the early liquid interaction with the right bottom corner of the second-layer particle breaks the one large capillary meniscus into two smaller capillary menisci, which enhance the vertical and horizontal capillary flows through the right and bottom pores next to the second-layer particle as shown in Fig. 8(e) at $t^* = 119$ due to the larger capillary pressure, i.e., smaller capillary menisci. At $t^* = 130$ and 150, Fig. 8 (f) and (g) shows the quick capillary fillings through the pores near the second-layer particle, and the smaller pore near the right plate enhances the vertical capillary flow. At $t^* = 480$, Fig. 8(h) shows that the decreased capillary pressure due to the pinning of the left and right menisci is lower than the hydrostatic pressure, i.e., the liquid front reaches equilibrium state, and the left meniscus is slightly higher than the right meniscus due to the larger flow area.

Fig. 9(a) and (b) compares the LBM predicted maximum and minimum dimensionless liquid heights, $h_{max}{}^*$, and $h_{min}{}^*$, respectively, as a function of dimensionless time, t^*, for the single-column-particle uniform and non-uniform pore size wicks Case A1 ($l_r = 1$) and Case A2 ($l_r = 1.3$) at given parallel plate spacing and porosity, $W = 100\ \delta x$ and $\varepsilon = 0.67$, respectively, including the elapsed time label for the rate-of-rise snapshots given in Fig. 8(a)–(h).

The initial sharp rate-of-rise is very similar between Cases A1 and A2, i.e., [see Fig. 8(a) or point (a)]. However, starting from point (b), i.e., $t^* = 21$, the maximum liquid height for Case A2 begins to show the moderate enhancement compared to Case A1 until it reaches point (c), i.e., $t^* = 105$, while the minimum liquid height for both cases is at the top surface of the first particle (pinning followed by stick-slip flow).

At point (d), i.e., $t^* = 110$, the meniscus-particle interaction results in the sharp rate-of-rise in the maximum liquid height, however, it takes time for the minimum height to rise because the liquid needs to fill the pore between two particles, i.e., Fig. 8(e) at $t^* = 119$. At $t^* = 130$, i.e., Fig. 8(f), Case A2 yields the sharp rate-of-rise for both minimum and

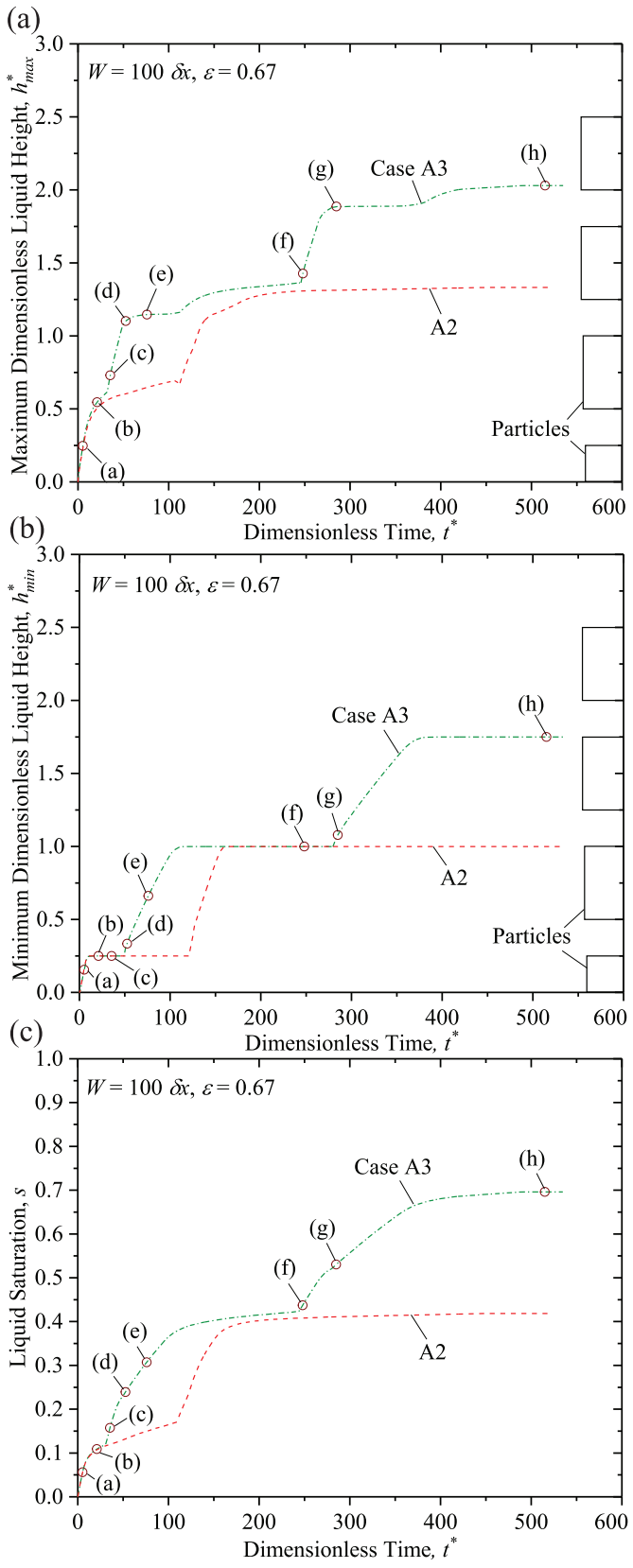

Fig. 11. (a) Maximum dimensionless liquid height, h_{max}*, (b) minimum dimensionless liquid height, h_{min}*, and (c) liquid saturation, s, as a function of dimensionless time, t*, for non-uniform wick with $l_r = 1.3$ (Case A2) and $l_r = 2.6$ (Case A3) at given porosity ($\varepsilon = 0.67$) and parallel plate spacing ($W = 100\ \delta x$).

maximum liquid height in the large and small pores near the second-layer particle, respectively. At $t^* = 150$, Fig. 8(g) shows that the maximum liquid height is pinned, while the minimum liquid height is about to reaching the particle top surface level. At $t^* = 480$, i.e., point (h), the maximum and minimum dimensionless liquid height have reached equilibrium state, as shown in Fig. 9(a) and (b), respectively.

Fig. 9(c) shows the liquid saturation, s, for Cases A1 and A2. The non-uniform wick, i.e., Case A2, allows for the early step-wise liquid height increase compared to that of Case A1 at $t^* = 110$, point (d), due to the early interaction between the liquid and second-layer particle, followed by the enhanced capillary pressure from the smaller capillary menisci through the smaller pores near the second-layer particle, i.e., points (e) to (g). The liquid saturation for Case A2 shows the marginally-increased equilibrium height, i.e., point (h), due to the minor maximum liquid height increase in the large pore, i.e., the marginally-extended meniscus crescent.

4.3. Non-uniform pore size wick: pore size ratio effect

This section studies the effects of non-uniform pore size ratio on enhanced wickability by comparing rate-of-rise for Case A2 ($l_r = 1.3$ with Case A3 ($l_r = 2.6$) at given porosity $\varepsilon = 0.67$ Fig. 10.(a)–(h) shows the LBM rate-of-rise snapshots for Case A3 [see

Fig. 5 Fig. 10.(a), i.e., $t^* = 5.4$, illustrates the larger rate-of-rise in the large pore, i.e., the pore between the first layer particle and the right plate, due to the larger permeability compared to the left pore. At $t^* = 21$, Fig. 10(b) shows that the enhanced capillary flow continues through the large pore, while the meniscus pinning occurs at the right top corner of the first-layer particle. At $t^* = 36$, Fig. 10(c) shows the early capillary meniscus-particle corner interaction which results in the enhanced capillary flow rise, followed by the second sharp rate-of rise through the smaller pore as shown in Fig. 10(d) and (e), i.e., $t^* = 53$ and 76. This higher rate-of-rise in Case A3 ($l_r = 2.6$), compared to Case A2 [$l_r = 1.3$, Fig. 8(c)–(f)], results from the earlier liquid-particle corner interaction by the larger pore size ratio. At $t^* = 248$, Fig. 10(f) shows the third sharp rate-of-rise, since the capillary meniscus interacts with the bottom corner of the third particle.

At $t^* = 285$, Fig. 10(g) shows that the meniscus in the small pore has already reached the top surface of the third-layer particle, while the right capillary meniscus fills the pore between the third-layer particle and right plate Fig. 10.(h), i.e., $t^* = 515$, shows that the decreased capillary pressure due to the pinning of the left and right menisci is lower than the hydrostatic pressure, i.e., equilibrium state is reached.

Fig. 11(a) and (b) compares the LBM predicted maximum and minimum dimensionless liquid heights, h_{max}*, and h_{min}*, respectively, as a function of dimensionless time, t*, for two non-uniform wicks with different pore size ratios, $l_r = 1.3$ (Case A2) and $l_r = 2.6$ (Case A3), at given parallel plate spacing and porosity, $W = 100\ \delta x$ and $\varepsilon = 0.67$, respectively, including the elapsed time label for the rate-of-rise snapshots given in Fig. 10(a)–(h). The maximum liquid height for Case A3 shows the enhancement at $t^* = 21$ and 36 [see Fig. 10(b) and (c) or points (b) and (c)] compared to Case A2, due to the earlier interaction between the liquid and right bottom corner of the second-layer particle. However, the minimum liquid height for Case A3 is same as those for Case A2 until at $t^* = 53$, i.e., point (d), since the two menisci pin at the top corners of the first-layer particle. At point (d), the left meniscus finally detaches from the top surface of the first-layer particle after filling the pore between the first- and second-layer particles, while the right meniscus has already reached the level of the top surface of the second-layer particle due to the high capillary pressure from the small pore with the left side of the meniscus pinned at the particle top right corner and the right side rising slowly at the right plate inner surface. At $t^* = 76$, i.e., point (e), Fig. 11(a) shows the small rate-of-rise of the maximum liquid height due to the reduced capillary pressure from meniscus pinning at the second particle top right corner, while Fig. 11 (b) shows that the minimum liquid height quickly rises near the second-

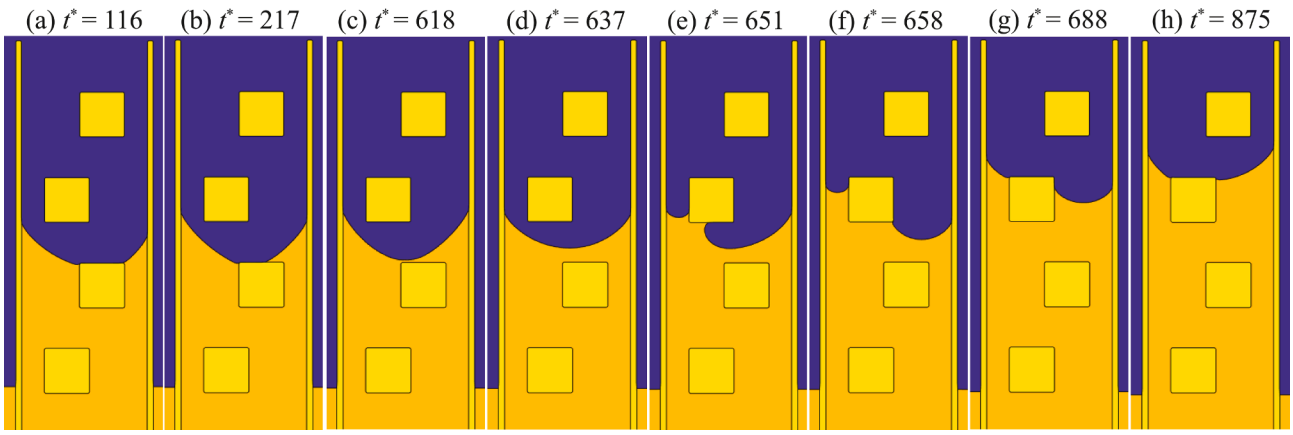

Fig. 12. Snapshots of rate-of-rise in single-column uniform pore size wick with $\varepsilon = 0.8$ and $l_r = 2.6$ (Case B3) from (a) $t^* = 116$ to (h) the equilibrium state $t^* = 875$. The dimensionless time, t^*, corresponding to each snapshot is also shown.

layer particle, i.e., second sharp rate-of-rise. Similarly, $t^* = 248$ corresponds to the third sharp maximum liquid rate-of-rise, as shown at point (f) in Fig. 11(a), and $t^* = 285$ is associated with the meniscus detachment and the third sharp rate-of-rise for the minimum liquid height as shown at point (g) in Fig. 11(b).

At $t^* = 515$, Fig. 11(a) and (b) shows that the maximum and minimum liquid heights reach the equilibrium condition with 52.4% and 75% enhancement compared to that of Case A2, respectively, resulting from the larger pore size ratio compared to Case A2 Fig. 11.(c) shows the liquid saturation, s, as a function of dimensionless time, t^*, for Cases A2 and A3. The non-uniform wick with the higher pore size ratio, i.e., Case A3, shows not only the larger saturation level at $t^* = 36$–76, i.e., points (c)–(e), but also the larger saturation beyond point (f), since the smaller pores near the plates offer the early capillary rise from the enhanced liquid-surface interaction and increase the capillary pressure via a smaller effective capillary meniscus radius.

4.4. Non-uniform pore size wick: porosity effect

This section examines the effects of porosity on the enhanced wickability of non-uniform pore size wicks by comparing the rate-of-rise for Case A3 ($\varepsilon = 0.67$) and Case B3 ($\varepsilon = 0.8$) at given pore size ratio, $l_r = 2.6$.

Fig. 12(a)–(h) shows the LBM snapshots for Case B3 [see Fig. 5] from $t^* = 116$ to 875 (equilibrium state). The rate-of-rise and capillary front movement are similar between Cases A3 and B3 until $t^* = 116$, i.e., Fig. 12(a), where both the left and right menisci reach the same level of the second-particle top surface. However, compared to Case A3, Case B3 decreases the rate-of-rise due to the poor interaction between the left meniscus and left bottom corner of the third-layer particle resulting from the larger pore between the second- and third-layer particles and between the third-layer particle and the left plate. However, the right meniscus depinnes from the top right corner of the second-layer particle due to the large capillary pressure from the small pore between the second-layer particle and the right plate, and slowly flows over the top surface of the particle, i.e., stick-slip flow, shown by Fig. 12(b), i.e., $t^* = 217$. The extended slow stick-slip flow continues until $t^* = 618$, i.e., Fig. 12(c), where the right meniscus bridges with the left meniscus to form a new meniscus between the two parallel plates. At $t^* = 637$, Fig. 12(d) shows that the meniscus rises between the parallel plates. At $t^* = 651$, Fig. 12(d) shows that the meniscus interacts with the particle, followed by the sharp rate-of-rise at $t^* = 658$ and 688, i.e., Fig. 12(f) and (g). At $t^* = 875$, Fig. 12(h) shows the two menisci pinned at the top corners of the third-layer particle, i.e., equilibrium state has reached.

Fig. 13(a) and (b) compare the LBM predicted maximum and minimum dimensionless liquid heights, $h_{max}{}^*$, and $h_{min}{}^*$, respectively, as a function of dimensionless time, t^*, for Cases A3 and B3, and the rate-of-rise behaviors are very similar at $t^* < 217$. Beyond point (b), Case B3 shows the delayed rate-of-rise due to the lateral stick-slip flow from $t^* = 217$ to $t^* = 618$, i.e., points (b) to (c), which is associated with the poor interaction between the meniscus front and left bottom corner of the third-layer particle from the larger pores around. This is followed by the two menisci merge and rise, i.e., points (c) and (d), and the meniscus interaction with the third particle resulting in the third sharp rate-of-rise, i.e., points (e) to (g). At $t^* = 875$, i.e., point (h), the menisci reach the top level of the third-layer particle and the equilibrium state is reached.

Fig. 13(c) shows the liquid saturation, s, as a function of dimensionless time for Cases A3 and B3. At $t^* < 217$, i.e., points (a) and (b), Case B3 shows the moderately higher liquid saturation than that of Case A3, due to the larger permeability from the large pores (higher porosity). However, the larger pores also lower the capillary pressure, which in turn reduces the rate-of-rise including the delayed sharp rate-of-rise at $t^* > 618$, i.e., points (c) to (g). In other words, the reduced porosity of non-uniform wicks increases the rate-of-rise at given pore size ratio, which indicates the significant impact of the small pores on enhanced rate-of-rise. Eventually, both Cases reach a similar saturation at the equilibrium state. Note that the larger pore is expected to reduce the equilibrium height by lowering the capillary pressure, however, the pining effect is dominant over the capillary pressure difference (both minimum liquid heights sit near the top surface of third-layer particle), which results in the similar equilibrium height.

4.5. Non-uniform pore size wick: effects of decreasing pore size in the flow direction

The effects of upward stream-wise, non-uniform pore size distribution on enhanced wickability is investigated by comparing the rate-of-rise between horizontally non-uniform pore size wicks (Case A3) and horizontally/vertically non-uniform pore size wick (Case A4, see Fig. 5) at $\varepsilon = 0.67$ and $l_r = 2.6$. Fig. 14(a)–(h) shows the LBM rate-of-rise snapshots of Case A4. At $t^* = 93.2$, Fig. 14(a) shows that the right meniscus is about to interacting with the second-particle bottom right corner, while both menisci have already been depinned and slowly flow over the top surface of the first-layer particle, i.e., stick-slip flow. The left

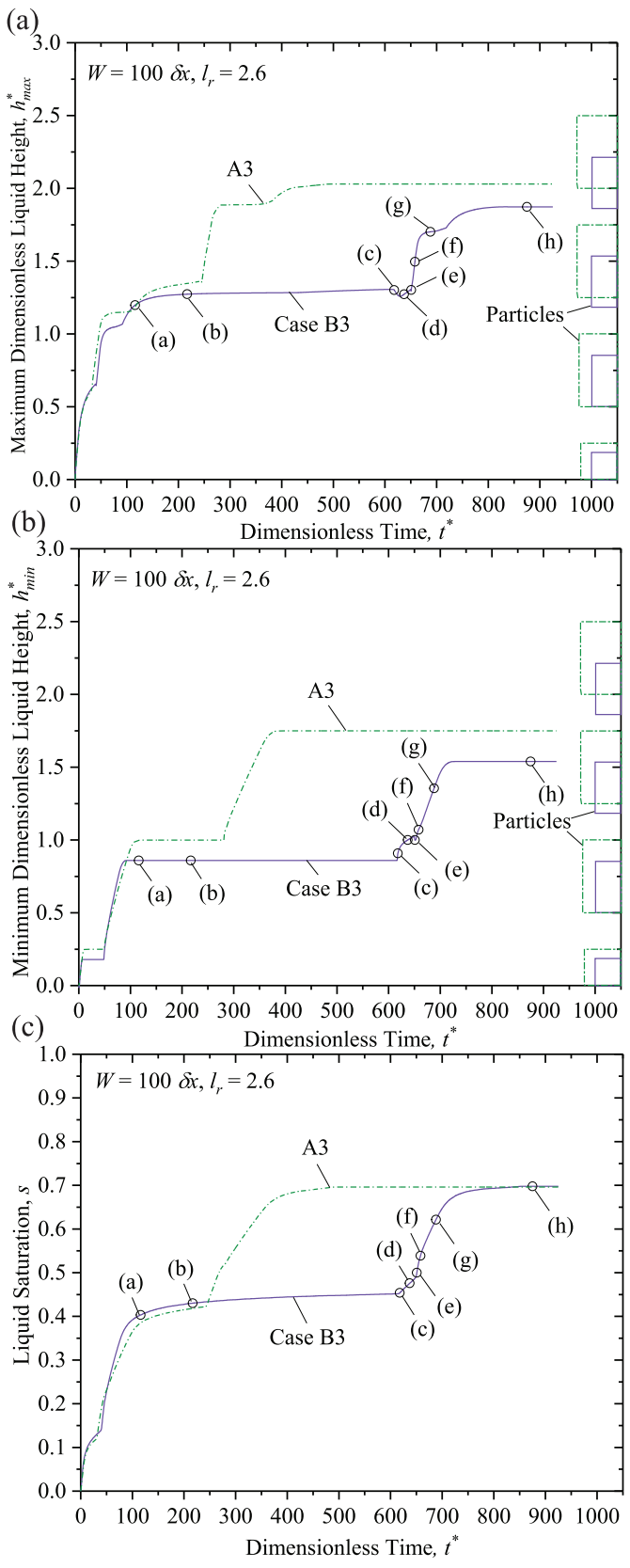

Fig. 13. (a) Maximum dimensionless liquid height, h_{max}*, (b) minimum dimensionless liquid height, h_{min}*, and (c) liquid saturation, s, as a function of dimensionless time, t*, for non-uniform wick with $\varepsilon = 0.67$ (Case A3) and $\varepsilon = 0.8$ (Case B3) at given pore size ratio ($l_r = 2.6$) and parallel plate spacing ($W = 100\ \delta x$).

meniscus spread over the top surface of the particle is more significant than the right meniscus spread, resulting from the larger capillary pressure from the small pore. Comparing with the sharp rate-of-rise at $t^* = 36$ for Case A3, i.e., Fig. 10(c), the large pore between the first- and second-layer particle for Case A4 slow down the rate-of-rise due to the relatively late meniscus-particle interaction. At $t^* = 113$, Fig. 14(b) shows that the right meniscus quickly rises to the top of the second particle due to the large capillary pressure from the small pore, while the left capillary meniscus fills the large pore between the first and second-layer particles and detaches from the top surface of the first-layer particle.

At $t^* = 358$, Fig. 14(c) shows that the left meniscus interacts with the bottom left corner of the third-layer particle, while the right meniscus has already depinned (due to the large capillary pressure from the small pore between the second-layer particle and the right plate) and is spreading over the top surface of the second-layer particle, i.e., stick-slip flow. At $t^* = 372$, Fig. 14(d) shows that the left capillary meniscus rises in the small pore between the third-layer particle and left plate, while the capillary meniscus between the second- and third-layer particles fills the pore. At $t^* = 422$, Fig. 14(e) shows the left capillary meniscus pins at the top left corner of the third-layer particle, while the right capillary meniscus rises between the third-layer particle and the right plate. At $t^* = 513$, Fig. 14(f) shows the right capillary meniscus rises quickly by interacting with the fourth-layer particle bottom right corner, i.e., early interaction from proximity to particle surface. At $t^* = 550$, Fig. 14(g) shows that the right and central menisci quickly fill the small pores due to the large capillary pressure. At $t^* = 900$, Fig. 14(h) shows the equilibrium condition with both menisci pinned at the fourth-layer particle top corners.

Fig. 15(a) and (b) compares the LBM predicted maximum and minimum dimensionless liquid heights, h_{max}*, and h_{min}*, respectively, as a function of dimensionless time, t*, for the stream-wise, uniform (Case A3) and non-uniform, i.e., decreasing (Case A4) pore size wicks with horizontally non-uniform pore size distribution at given porosity, $\varepsilon = 0.67$, pore size ratio, $l_r = 2.6$, and parallel plate spacing, $W = 100\ \delta x$, including the elapsed time label for the rate-of-rise snapshots given in Fig. 14(a)–(h). While the overall pattern (or trend) of rate-of-rise is similar between Cases A3 and A4 form initial time, i.e., $t^* = 0$ to point (f), i.e., $t^* = 513$, i.e., similar periods of sharp rate-of-rise and plateaus, the maximum and minimum liquid heights for Case A4 are slightly behind those of Case A3 due to larger pore size in the bottom side of the wick. More specifically, the larger pores in the bottom side of the wick does not promote early meniscus-particle interaction, which can be observed in point (a), i.e., meniscus interaction with the second-layer particle, and in point (c), i.e., meniscus interaction with the third-layer particle, i.e., $t^* = 93.2$ and $t^* = 358$, respectively (compare with Fig. 10(c) and (f), i.e., snapshots of Case A3 at $t^* = 36$ and $t^* = 248$, respectively). Contrary to Case A3 in which the liquid reaches equilibrium state at around the level of the top surface of the third particle, for Case A4 the maximum liquid height experiences the third sharp rate-of-rise through interaction with the fourth-layer particle at $t^* = 513$, i.e., point (f). At point (g), i.e., $t^* = 550$, the maximum liquid height has reached the fourth and final plateau while the minimum height is about to experience the fourth sharp rate-of-rise after detaching from the top surface of the third-layer particle. Point (h), i.e., $t^* = 900$, corresponds to the equilibrium state for both maximum and minimum liquid heights. From initial time to point (f), i.e., $t^* = 0$ to $t^* = 513$, liquid saturation of neither cases have superiority over the other resulting from the competing effects of increased capillary pressure from small pore for Case A3 and increased permeability from the large pores for Case A4, however, beyond point (f), liquid saturation for Case A4 continues to rise above those of Case A3 due to liquid rise to the fourth particle resulting from increased capillary pressure from the small pore on the top side of the wick until it reaches equilibrium at point (h), i.e., $t^* = 900$.

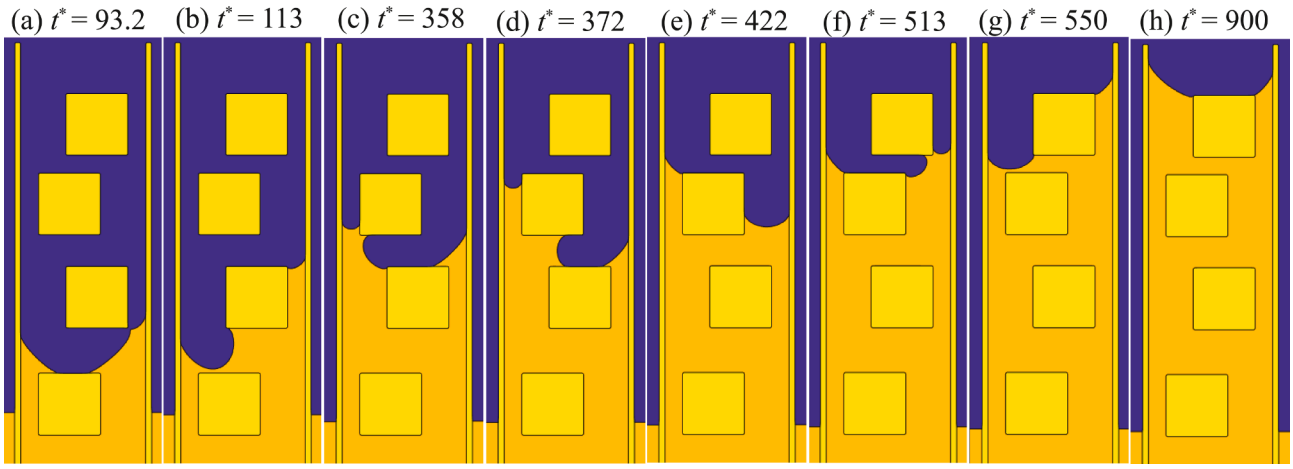

Fig. 14. Snapshots of rate-of-rise in single-column non-uniform pore size wick with non-uniform pore distribution in stream-wise direction with $\varepsilon = 0.8$ and $l_r = 2.6$ (Case A4) from (a) $t^* = 93.2$ to (h) the equilibrium state, i.e., $t^* = 900$. The dimensionless time, t^*, corresponding to each snapshot is also shown.

4.6. Summary of the enhanced wickability of non-uniform wicks

To further evaluate the wickability enhancement of non-uniform wicks compared to the uniform wicks, three new parameters are introduced, i.e., a maximum instantaneous rate-of-rise enhancement, a cumulative (time integration) rate-of-rise enhancement, and a capillary pressure (equilibrium height) enhancement. The predicted cumulative and maximum instantaneous rate-of-rise and capillary pressure enhancements of non-uniform pore size wicks are summarized in Table 4 as well as the dimensionless times at which the maximum instantaneous rate-of-rise enhancements occur. The maximum instantaneous rate-of-rise enhancement, ξ is calculated as

$$\xi = \max\left(\frac{\varphi(t^*)_{nu} - \varphi(t^*)_u}{\varphi(t^*)_u}\right) \tag{18}$$

where φ is either the maximum dimensionless liquid height, $h_{\max}{}^*$, minimum dimensionless liquid height, $h_{\min}{}^*$, or liquid saturation, s, respectively. The cumulative (time integrated) rate-of-rise enhancement, ω is given as

$$\omega = \frac{\int_0^{t^*_{eq}} \varphi(t^*)_{nu} \mathrm{d}t^* - \int_0^{t^*_{eq}} \varphi(t^*)_u \mathrm{d}t^*}{\int_0^{t^*_{eq}} \varphi(t^*)_u \mathrm{d}t^*} \tag{19}$$

where t^*_{eq} is the dimensionless time for the equilibrium height. The equilibrium dimensionless time is determined at the time when both the maximum and minimum dimensionless heights become constant over at least 100 dimensionless time periods, i.e., $\Delta t^* > 100$, as the predicted dimensionless equilibrium height h^*_{eq} and time t^*_{eq} are found in Table 4. Note that the dimensionless equilibrium height refers to the dimensionless minimum equilibrium height. Also, the wicks with the smaller porosity at given pore size ratio, i.e., A2-A4 reaches the equilibrium state earlier than the counter parts, i.e., B2-B4, due to the enhanced rate-of-rise from the presence of the smaller pores. However, we use the larger equilibrium time to calculate the cumulative rate-of-rise enhancements of the non-uniform wicks using Eq. (19) with $t^*_{eq} = 490$ for Cases A2 and B2, $t^*_{eq} = 875$ for Cases A3 and B3, and $t^*_{eq} = 1400$ for Cases A4 and B4.

Also, note that the t^*_{eq} increases as the equilibrium height increases at given porosity, i.e., t^*_{eq} (Case A4) > t^*_{eq} (Case A3) > t^*_{eq} (Case A2) and t^*_{eq} (Case B4) > t^*_{eq} (Case B3) > t^*_{eq} (Case B2).

The maximum capillary pressure enhancement, γ is predicted as

$$\gamma = \frac{\varphi(t^*)_{nu,eq} - \varphi(t^*)_{u,eq}}{\varphi(t^*)_{u,eq}} \tag{20}$$

where φ is either the maximum dimensionless liquid height, $h^*_{\max}$, minimum dimensionless liquid height, $h^*_{\min}$, or liquid saturation, s at equilibrium state, respectively.

For Case A2, the maximum instantaneous rate-of-rise enhancement is found at the minimum dimensionless liquid height $t^* = 136$, $\xi = 180\%$, resulting from the early meniscus-particle corner interaction [see Fig. 8 (f), left pore near second layer particle]. This maximum instantaneous enhancement is found at the maximum relative height difference where the sharp rate-of-rise occurs in the non-uniform wick, and this height difference is more pronounced for the minimum liquid height than the maximum liquid height. The cumulative rate-of-rise enhancements, on the other hand, are relatively small, i.e., $\omega \leq 7\%$, mainly due to the minor equilibrium height increase, i.e., $\gamma \leq 2\%$. For Case B2, the maximum instantaneous rate-of-rise enhancements are much smaller than those of Case A2, i.e., $11 \leq \xi \leq 18\%$, due to the smaller rate-of-rise from the presence of the large pores. The cumulative rate-of-rise enhancement and capillary pressure enhancement are likewise very small, i.e., $\omega \leq 2\%$ and $\gamma \leq 2\%$, respectively. Similar observation is found for Case B3 vs A3, and Case B4 vs A4, i.e., the enhanced wickability of the non-uniform wicks decreases as the porosity increases at given pore size ratio. Note the maximum instantaneous rate-of-rise enhancements for all cases are much larger than the cumulative rate-of-rise enhancements, since the cumulative rate-of-rise reflects the time integrated enhancement, i.e., time average over the entire rate-or-rise period.

For Case A3, the maximum instantaneous rate-of-rise enhancement is found at the minimum dimensionless liquid height $t^* = 129$, $\xi = 298\%$, which is larger than that of Case A2 due to the larger permeability and capillary pressure from the larger and smaller pores, respectively [no snapshot is given but it occurs in the left pore near second-layer particle somewhere between Fig. 10(e) and (f)]. The Case A3 cumulative rate-of-rise enhancements are much larger than Case A2, i.e., $51 \leq \omega \leq 65\%$, resulting from enhanced capillary pressure (or equilibrium height), i.e.,

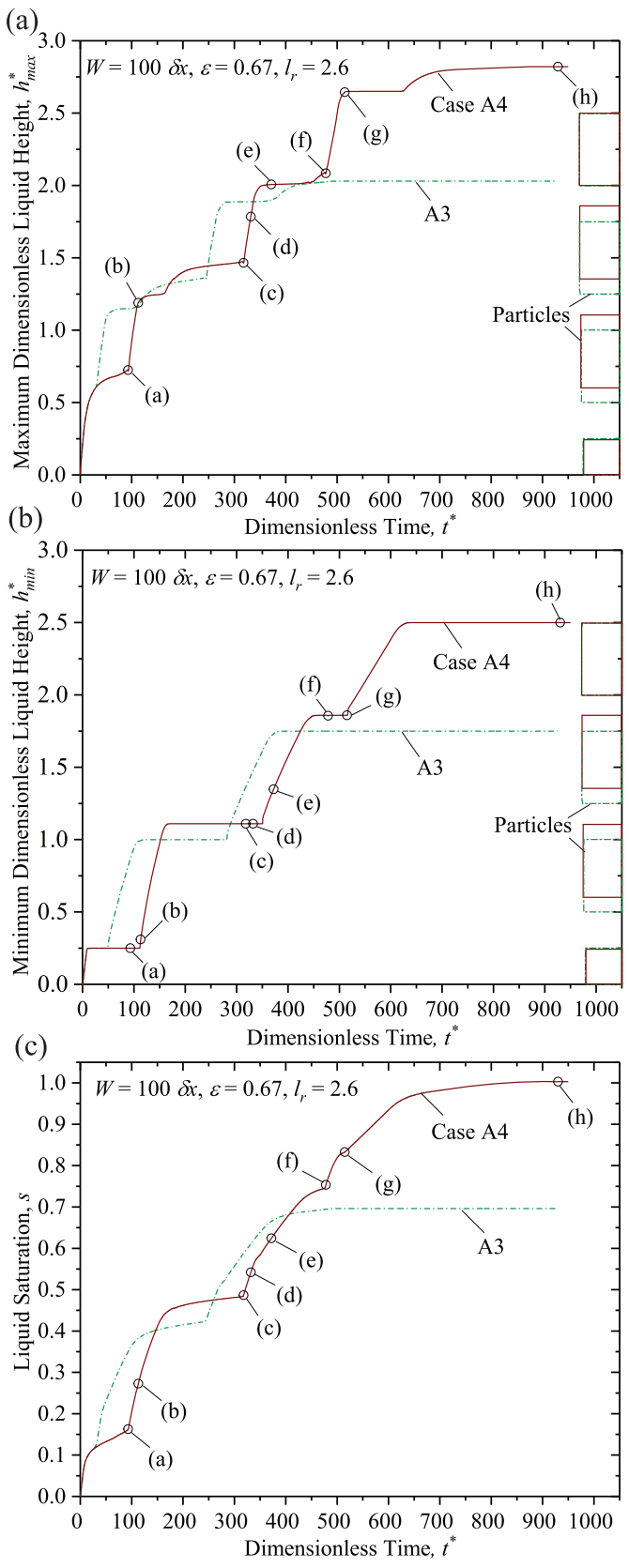

Fig. 15. (a) Maximum dimensionless liquid height, $h$max*, (b) minimum dimensionless liquid height, $h$min*, and (c) liquid saturation, s, as a function of dimensionless time, t*, for stream-wise uniform (Cases A3) and non-uniform, i.e., decreasing (Cases A4) pore size wicks with horizontally non-uniform pore size distribution at given porosity ($\varepsilon = 0.67$), pore size ratio ($lr = 2.6$), and parallel plate spacing ($W = 100\ \delta\xi$).

$55 \leq \gamma \leq 75$ (up to 75% for minimum height), due to the presence of small pores. For Case B2, the maximum instantaneous rate-of-rise enhancements is found at the minimum dimensionless liquid height $t^* = 65$, $\xi = 244\%$, and the cumulative enhancements are up to 27% due to the enhanced capillary pressure from the small pores (up to 79% for minimum height). For Case A4, the maximum instantaneous rate-of-rise enhancement is found at the minimum dimensionless liquid height $t^* = 136$, $\xi = 228\%$ [no snapshot is given, but it occurs in the left pore near second-layer particle somewhere between Fig. 14(b) and (f)]. This enhancement is slightly smaller than the maximum instantaneous rate-of-rise enhancement of Case A3 ($\xi = 298\%$), due to the smaller rate-of-rise from the larger pores in the bottom side of the wick in Case A4. On the other hand, the cumulative rate-of-rise enhancement is up to 114% for the minimum height, which is the largest among all cases. This results from the large capillary pressure enhancement (up to 150% for the minimum height), due to the presence of the small pores in the top side of the wick.

For Case B4, the maximum instantaneous rate-of-rise enhancement occurs at equilibrium time, i.e., $t^* = 1400$, $\xi = 157\%$ (for minimum height), due to the small rate-of-rise from the large pores in the bottom side of the wick. The cumulative rate-of-rise enhancements are found up to 65% (for minimum height) due to the enhanced capillary pressure (or equilibrium height), i.e., $106 \leq \gamma \leq 157$ (up to 157% for minimum height), due to presence of the small pores in the top side of the wick.

5. Conclusion

This study examines the enhanced wickability of the non-uniform pore size wicks by employing the free-energy-based, single-component, two-phase Lattice Boltzmann Method (LBM). The single-column, four-layer, uniformly/non-uniformly distributed square particles within the two parallel plates are considered with the variations of the porosity, pore-size ratio, and stream-wise pore-size distribution. The enhanced wickability is predicted by calculating the instantaneous and time-integral enhancements of the liquid heights and saturation as well as the capillary pressure enhancement of the non-uniform pore wicks. The main conclusions are summarized below.

- Compared to the uniform pore wick, all the non-uniform pore wicks enhance the wickability by increasing the permeability from the large pores and improving the capillary pressure from the small pores. The enhancement increases as the pore size ratios increase at given porosity or the porosity decreases at given pore size ratio.
- The non-uniform wicks with small pore size ratio ($l_r = 1.3$) show the large maximum instantaneous rate-of-rise enhancement, i.e., up to 180 and 18% at porosity of 0.67 and 0.8, respectively, but only marginal cumulative rate-of-rise enhancement, i.e., $< 7\%$ due to the similar small pore size for capillary pressure improvement.
- The non-uniform wicks with large pore size ratio ($l_r = 2.6$) show not only the large maximum instantaneous rate-of-rise enhancement, i.e., up to 298 and 244% at porosity of 0.67 and 0.8, respectively, but also the large cumulative rate-of-rise enhancement, i.e., up to 65 and 27%, due to the improved permeability from the large pores and enhanced capillary pressure from the small pores.
- The non-uniform wicks with high pore size ratio and decreasing pore size in the flow direction show the best overall performance mainly due to the smaller pores in the top side of the wick that gradually increase the capillary pressure as the liquid flows, i.e., the capillary pressure gradually increases to compensate the increasing hydrostatic pressure. The maximum instantaneous and cumulative rate-of-rise enhancement and capillary pressure enhancement are found to be up to 228, 114, and 150% at porosity of 0.67 and 157, 65, and 157% at porosity of 0.8, respectively.
- The rate-of-rise shows the step-wise capillary meniscus front increase, i.e., sharp rate-of-rise followed by periods of slow rate-of-rise due to the meniscus pinning and stick-slip flow. Further studies on

Table 4
Equilibrium height h^*_{eq} and time, t^*_{eq}, cumulative and maximum instantaneous rate-of-rise enhancements and capillary pressure (equilibrium height) enhancement of the maximum dimensionless liquid height, h^*_{max}, minimum dimensionless liquid height, h^*_{min}, and liquid saturation, s, for all the non-uniform wicks compared to the corresponding uniform wicks, i.e., Cases A2–A4 compared to Case A1 ($\varepsilon = 0.67$), and Cases B2–B4 compared to Case B1 ($\varepsilon = 0.8$). The dimensionless time, t^*, corresponding to each of the maximum instantaneous enhancements are also shown.

Rate-of-Rise Enhancement,%										
Case #	h^*_{eq} at t^*_{eq}	Maximum Instantaneous, ξ			Cumulative, ω			Capillary Pressure,γ		
		h^*_{max} at t^*	h^*_{min} at t^*	s at t^*	h^*_{max}	h^*_{min}	s	h^*_{max}	h^*_{min}	s
A2	1 at 480	95 at 155	180 at 136	82 at 146	7	5	6	2	0	2
B2	0.86 at 490	18 at 94	18 at 90	11 at 90	2	0	1	2	0	1
A3	1.75 at 515	118 at 155	298 at 129	126 at 103	51	65	62	55	75	70
B3	1.54 at 875	69 at 73	244 at 65	93 at 66	21	26	27	54	79	69
A4	2.5 at 900	114 at 900	228 at 136	142 at 900	90	114	112	116	150	145
B4	2.2 at 1400	106 at 1400	157 at 1400	137 at 1400	46	65	61	106	157	137

the capillary pressure changes during the pining/depining/stick-slip flow processes are needed.
- This study employs the simple square particles for the simplicity without losing a generality of the nonuniform pore size. The obtained results provide deep insights into the optimal wick designs and manufacturing for the enhanced wickability.
- The obtained enhanced wickability mechanism in the present 2D simulation may be a bit different from that of 3D non-uniform pore-size network due to the different capillary flow path and wetting mechanisms from the different geometrical pore connectivity and pore surface curvatures. The detailed enhanced wickability mechanisms in 3D will be examined in future study.

CRediT authorship contribution statement

Mohammad Borumand: Methodology, Investigation, Software, Writing – original draft. **Taehun Lee:** Methodology, Investigation, Software, Writing – review & editing. **Gisuk Hwang:** Conceptualization, Supervision, Funding acquisition, Writing – review & editing.

Declaration of Competing Interest

The authors declare that they have no known competing financial interests or personal relationships that could have appeared to influence the work reported in this paper.

Acknowledgments

MB and GS are thankful for financial support by the National Science Foundation (NSF), Award No. OIA-1929187, and the Wichita State University Convergence Sciences Initiative Program, and the College of Engineering, Department of Mechanical Engineering, Wichita State University.

Appendix

Particle (or Pore) Size Sensitivity

A particle (or a pore) size sensitivity is examined to determine the minimum pore and particle sizes for LBM simulation by changing the pore and particle sizes, $l_p = 10, 12, 14, 16\ \delta x$ as shown in Fig. A1. To represent the same rate-of-rise simulations with the different pore and particle sizes, the Bond and Ohnesorge numbers are fixed by changing the gravitational acceleration and dynamic viscosity, which are given in Eqs. (A.1) and (A.2)

$$Bo = \frac{\Delta\rho g {l_p}^2}{\sigma} = \left(\frac{l_p}{L_c}\right)^2 \tag{A.1}$$

$$Oh = \frac{\mu}{\sqrt{\rho_l \sigma l_p}} \tag{A.2}$$

where $\Delta\rho$ is the density difference between the liquid and vapor, g is the gravitational acceleration, l_p is the characteristic pore and particle size, σ is the surface tension force, $L_c = \sqrt{\sigma/\Delta\rho g}$ is the capillary length, μ is the surface tension force, and ρ_l is the liquid density. The dynamic viscosity can be found using $\mu = \rho_l\lambda/3$, where λ is the relaxation time.

Fig. A1 shows the simulation setup including single column of uniformly arranged particles with uniform size for the particle (or pore) size sensitivity study.

Table A1 summarizes the 4 cases ($l_p = 10$, 12, 14, and 16 δx) simulated for the particle (or pore) size sensitivity study to ensure the reasonably large pore and particle sizes for the prescribed liquid-vapor interface thickness over 4 lattices.

Fig. A2 shows that the rate-of-rise and/or equilibrium height significantly change as the pore (or particle) size increases from $l_p = 10\ \delta x$ to $l_p = 14\ \delta x$, since the pore (or particle) size is not substantially large enough compared to the prescribed liquid-vapor interfacial thickness. Note that the case with $l_p = 10\ \delta x$ (Case C1) overpredicts the equilibrium height compared to the cases with $l_p = 14$ and 16 δx, and the cases with $l_p = 10\ \delta x$ (Case C1) and $l_p = 12\ \delta x$ (Case C2) shows higher rate-of-rise than the cases with $l_p = 14$ and 16 δx. However, the rate-of-rise and equilibrium height are nearly identical between $l_p = 14$ and 16 δx, which concludes that $l_p = 14\ \delta x$ is large enough to reasonably predict the capillary flow. Therefore, $l_p = 14\ \delta x$ is the minimum pore and particle size in the LBM simulation.

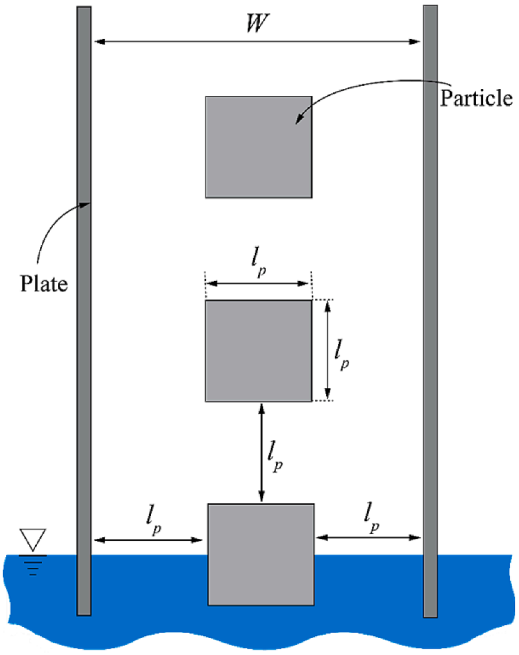

Fig. A1. A schematic of two parallel plates filled with single-column, uniform particles for lattice sensitivity study. The pore or particle sizes, l_p and width of the two plates, W are also shown.

Table A1
Two parallel plates with a single column of particles for particle (or pore) size sensitivity (Cases C1–C4).

	Magnitude, Lattice Unit			
Simulation parameter	Case C1	C2	C3	C4
W	30	36	42	48
l_p	10	12	14	16
$g\times10^6$	1.28	0.89	0.65	0.5
L	0.40	0.43	0.47	0.5
h_0	30	36	42	48
h_1	90	108	126	136
w_1	180	216	298	360
L_x	390	468	546	696
L_y	236	298	322	360

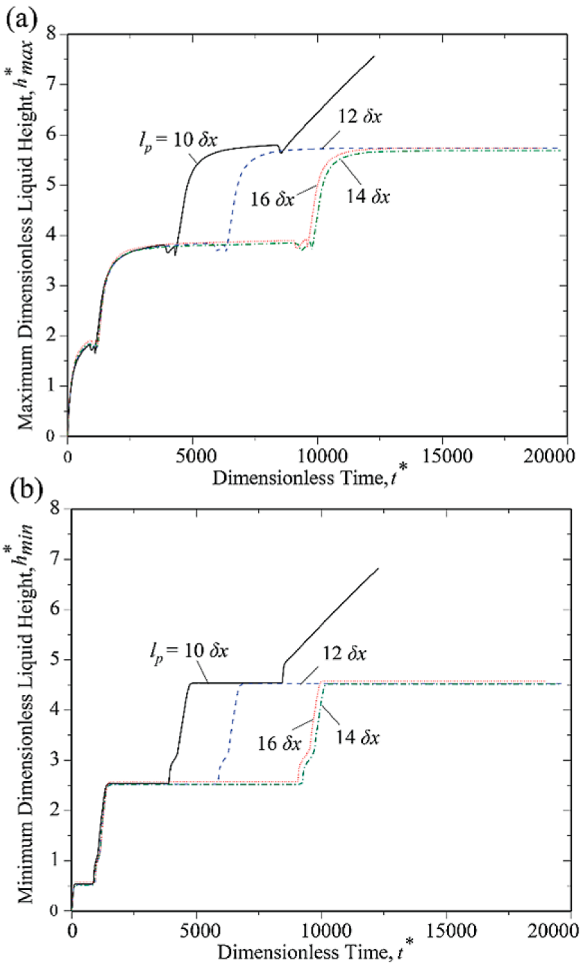

Fig. A2. (a) Maximum dimensionless liquid height, h_{max}* and (b) minimum dimensionless liquid height, h_{min}*, as a function of dimensionless time, t*, for four different characteristic pore and particle sizes, i.e., l_p = 10, 12, 14, and 16 δx.

References

[1] Mudawar I. Assessment of high-heat-flux thermal management schemes. IEEE Trans Compon Packag Technol 2001;24:122–41. https://doi.org/10.1109/6144.926375.

[2] Faghri A. Heat pipe science and technology. Taylor & Francis; 1995.

[3] Faghri A. Review and advances in heat pipe science and technology. J Heat Transf 2012;134. https://doi.org/10.1115/1.4007407.

[4] Li C, Peterson GP. Evaporation/boiling in thin capillary wicks (II)—effects of volumetric porosity and mesh size. J Heat Transf 2006;128:1320–8. https://doi.org/10.1115/1.2349508.

[5] Wang Y, Cen J, Jiang F, Cao W, Guo J. LHP heat transfer performance: a comparison study about sintered copper powder wick and copper mesh wick. Appl Therm Eng 2016;92:104–10. https://doi.org/10.1016/j.applthermaleng.2015.08.109.

[6] Ranjan R, Murthy JY, Garimella SV, Vadakkan U. A numerical model for transport in flat heat pipes considering wick microstructure effects. Int J Heat Mass Transf 2011;54:153–68. https://doi.org/10.1016/j.ijheatmasstransfer.2010.09.057.

[7] Ranjan R, Murthy JY, Garimella SV. A microscale model for thin-film evaporation in capillary wick structures. Int J Heat Mass Transf 2011;54:169–79. https://doi.org/10.1016/j.ijheatmasstransfer.2010.09.037.

[8] Deng D, Liang D, Tang Y, Peng J, Han X, Pan M. Evaluation of capillary performance of sintered porous wicks for loop heat pipe. Exp Therm Fluid Sci 2013;50:1–9. https://doi.org/10.1016/j.expthermflusci.2013.04.014.

[9] Deng D, Tang Y, Huang G, Lu L, Yuan D. Characterization of capillary performance of composite wicks for two-phase heat transfer devices. Int J Heat Mass Transf 2013;56:283–93. https://doi.org/10.1016/j.ijheatmasstransfer.2012.09.002.

[10] Byon C, Kim SJ. The effect of the particle size distribution and packing structure on the permeability of sintered porous wicks. Int J Heat Mass Transf 2013;61:499–504. https://doi.org/10.1016/j.ijheatmasstransfer.2013.02.025.

[11] Kim SJ, Ki Seo J, Hyung Do K. Analytical and experimental investigation on the operational characteristics and the thermal optimization of a miniature heat pipe with a grooved wick structure. Int J Heat Mass Transf 2003;46:2051–63. https://doi.org/10.1016/S0017-9310(02)00504-5.

[12] Chen SW, Hsieh JC, Chou CT, Lin HH, Shen SC, Tsai MJ. Experimental investigation and visualization on capillary and boiling limits of micro-grooves made by different processes. Sens Actuators Phys 2007;139:78–87. https://doi.org/10.1016/j.sna.2007.03.009.

[13] Semenic T, Catton I. Experimental study of biporous wicks for high heat flux applications. Int J Heat Mass Transf 2009;52:5113–21. https://doi.org/10.1016/j.ijheatmasstransfer.2009.05.005.

[14] Byon C, Kim SJ. Capillary performance of bi-porous sintered metal wicks. Int J Heat Mass Transf 2012;55:4096–103. https://doi.org/10.1016/j.ijheatmasstransfer.2012.03.051.

[15] Albu N., Keese J., Hwang G. Bimodal, thin wick structures for high heat flux two-phase thermal control systems 2019.

[16] Egbo M, Nasersharifi Y, Hwang G. Phase-change heat transfer of sintered-particle wick in downward facing orientation: particle size and wick thickness effects. Int J Heat Mass Transf 2020;155:119840. https://doi.org/10.1016/j.ijheatmasstransfer.2020.119840.

[17] Zhou W, Li Y, Chen Z, Deng L, Gan Y. A novel ultra-thin flattened heat pipe with biporous spiral woven mesh wick for cooling electronic devices. Energy Convers Manag 2019;180:769–83. https://doi.org/10.1016/j.enconman.2018.11.031.

[18] Wang B, Hong Y, Wang L, Fang X, Wang P, Xu Z. Development and numerical investigation of novel gradient-porous heat sinks. Energy Convers Manag 2015;106:1370–8. https://doi.org/10.1016/j.enconman.2015.10.071.

[19] Dai H, Chen W, Dong X, Liu Y, Cheng Q. Thermohydraulic performance analysis of graded porous media microchannel with microencapsulated phase change material suspension. Int J Heat Mass Transf 2021;176:121459. https://doi.org/10.1016/j.ijheatmasstransfer.2021.121459.

[20] Montessori A, Falcucci G. Lattice Boltzmann modeling of complex flows for engineering applications. Morgan & Claypool Publishers; 2018.

[21] Krastev VK, Falcucci G. Simulating engineering flows through complex porous media via the Lattice Boltzmann Method. Energies 2018;11:715. https://doi.org/10.3390/en11040715.

[22] Akhlaghi Amiri HA, Hamouda AA. Evaluation of level set and phase field methods in modeling two phase flow with viscosity contrast through dual-permeability

porous medium. Int J Multiph Flow 2013;52:22–34. https://doi.org/10.1016/j.ijmultiphaseflow.2012.12.006.
[23] Raeini AQ, Blunt MJ, Bijeljic B. Modelling two-phase flow in porous media at the pore scale using the volume-of-fluid method. J Comput Phys 2012;231:5653–68. https://doi.org/10.1016/j.jcp.2012.04.011.
[24] van der Hoef MA, Beetstra R, Kuipers JAM. Lattice-Boltzmann simulations of low-Reynolds-number flow past mono- and bidisperse arrays of spheres: results for the permeability and drag force. J Fluid Mech Camb 2005;528:233–54.
[25] Dorai F, Teixeira CM, Rolland M, Climent É, Marcoux M, Wachs A. Fully-resolved simulations of the flow through a packed bed of cylinders : effect of size distribution. Chem Eng Sci 2015;129:180. https://doi.org/10.1016/j.ces.2015.01.070.
[26] Nabovati A, Llewellin EW, Sousa ACM. A general model for the permeability of fibrous porous media based on fluid flow simulations using the Lattice Boltzmann Method. Compos Part Appl Sci Manuf 2009;40:860–9. https://doi.org/10.1016/j.compositesa.2009.04.009.
[27] Pan C, Hilpert M, Miller CT. Lattice-Boltzmann simulation of two-phase flow in porous media. Water Resour Res 2004;40. https://doi.org/10.1029/2003WR002120.
[28] Ebrahimi Khabbazi A, Ellis JS, Bazylak A. Developing a new form of the Kozeny–Carman parameter for structured porous media through lattice-Boltzmann modeling. Comput Fluids 2013;75:35–41. https://doi.org/10.1016/j.compfluid.2013.01.008.
[29] Gharibi F, Jafari S, Rahnama M, Khalili B, Jahanshahi Javaran E. Simulation of flow in granular porous media using combined Lattice Boltzmann Method and smoothed profile method. Comput Fluids 2018;177:1–11. https://doi.org/10.1016/j.compfluid.2018.09.020.
[30] Multiscale simulation of a novel leaf-vein-inspired gradient porous wick structure SpringerLink n.d. https://link.springer.com/article/10.1007/s42235-019-0100-x (accessed June 26, 2021).
[31] Huang H, Huang JJ, Lu XY. Study of immiscible displacements in porous media using a color-gradient-based multiphase Lattice Boltzmann Method. Comput Fluids 2014;93:164–72. https://doi.org/10.1016/j.compfluid.2014.01.025.
[32] Liu H, Valocchi AJ, Kang Q, Werth C. Pore-scale simulations of gas displacing liquid in a homogeneous pore network using the Lattice Boltzmann Method. Transp Porous Media 2013;99:555–80. https://doi.org/10.1007/s11242-013-0200-8.
[33] Liu H, Zhang Y, Valocchi AJ. Lattice Boltzmann simulation of immiscible fluid displacement in porous media: homogeneous versus heterogeneous pore network. Phys Fluids 2015;27:052103. https://doi.org/10.1063/1.4921611.
[34] Huang J, Xiao F, Yin X. Lattice Boltzmann simulation of pressure-driven two-phase flows in capillary tube and porous medium. Comput Fluids 2017;155:134–45. https://doi.org/10.1016/j.compfluid.2017.05.027.
[35] Falcucci G, Amati G, Krastev VK, Montessori A, Yablonsky GS, Succi S. Heterogeneous catalysis in pulsed-flow reactors with nanoporous gold hollow spheres. Chem Eng Sci 2017;166:274–82. https://doi.org/10.1016/j.ces.2017.03.037.
[36] Montemore MM, Montessori A, Succi S, Barroo C, Falcucci G, Bell DC, et al. Effect of nanoscale flows on the surface structure of nanoporous catalysts. J Chem Phys 2017;146:214703. https://doi.org/10.1063/1.4984614.
[37] Li Z, Galindo-Torres S, Yan G, Scheuermann A, Li L. Pore-scale simulations of simultaneous steady-state two-phase flow dynamics using a Lattice Boltzmann Model: interfacial area, capillary pressure and relative permeability. Transp Porous Media 2019;129:295–320. https://doi.org/10.1007/s11242-019-01288-w.
[38] Wang M, Xiong Y, Liu L, Peng G, Zhang Z. Lattice Boltzmann simulation of immiscible displacement in porous media: viscous fingering in a shear-thinning fluid. Transp Porous Media 2019;126:411–29. https://doi.org/10.1007/s11242-018-1162-7.
[39] Gu Q, Zhu L, Zhang Y, Liu H. Pore-scale study of counter-current imbibition in strongly water-wet fractured porous media using Lattice Boltzmann Method. Phys Fluids 2019;31:086602.
[40] Falcucci G, Amati G, Fanelli P, Krastev VK, Polverino G, Porfiri M, et al. Extreme flow simulations reveal skeletal adaptations of deep-sea sponges. Nature 2021;595:537–41. https://doi.org/10.1038/s41586-021-03658-1.
[41] Li J, Zheng W, Su Y, Hong F. Pore scale study on capillary pumping process in three-dimensional heterogeneous porous wicks using Lattice Boltzmann Method. Int J Therm Sci 2022;171:107236. https://doi.org/10.1016/j.ijthermalsci.2021.107236.
[42] Borumand M., Lee T., Hwang G. Enhanced wickability of thin non-uniform sintered particle wicks using Lattice Boltzmann Method, American Society of Mechanical Engineers Digital Collection; 2021. 10.1115/IMECE2020-24311.
[43] Albu N., Keese J., Hwang G. Bimodal, Thin wick structures for high heat flux two-phase thermal control systems 2019.
[44] Feng C, Yugeswaran S, Chandra S. Capillary rise of liquids in thermally sprayed porous copper wicks. Exp Therm Fluid Sci 2018;98:206–16.
[45] Lee T, Fischer PF. Eliminating parasitic currents in the lattice Boltzmann equation method for nonideal gases. Phys Rev E 2006;74. https://doi.org/10.1103/PhysRevE.74.046709.
[46] Lee T, Liu L. Wall boundary conditions in the lattice Boltzmann equation method for nonideal gases. Phys Rev E 2008;78:017702. https://doi.org/10.1103/PhysRevE.78.017702.
[47] Connington K, Lee T. Lattice Boltzmann simulations of forced wetting transitions of drops on superhydrophobic surfaces. J Comput Phys 2013;250:601–15. https://doi.org/10.1016/j.jcp.2013.05.012.
[48] He X, Shan X, Doolen GD. Discrete Boltzmann equation model for nonideal gases. Phys Rev E 1998;57:R13–6. https://doi.org/10.1103/PhysRevE.57.R13.
[49] Lee T, Lin CL. A stable discretization of the lattice Boltzmann equation for simulation of incompressible two-phase flows at high density ratio. J Comput Phys 2005;206:16–47. https://doi.org/10.1016/j.jcp.2004.12.001.
[50] Briant AJ, Yeomans JM. Lattice Boltzmann simulations of contact line motion. II. Binary fluids. Phys Rev E 2004;69:031603. https://doi.org/10.1103/PhysRevE.69.031603.
[51] Bosanquet CH. LV. On the flow of liquids into capillary tubes. Lond Edinb Dublin Philos Mag J Sci 1923;45:525–31. https://doi.org/10.1080/14786442308634144.
[52] Wolf FG, Dos Santos LO, Philippi PC. Capillary rise between parallel plates under dynamic conditions. J Colloid Interface Sci 2010;344:171–9.
[53] Wiklund HS, Uesaka T. Microfluidics of imbibition in random porous media. Phys Rev E Stat Nonlinear Soft Matter Phys 2013;87:023006. https://doi.org/10.1103/PhysRevE.87.023006.